

## FULL PAPER

# Solvent-assisted formation of ruthenium(II)/copper(I) complexes containing thiourea derivatives: Synthesis, crystal structure, density functional theory, enzyme mimetics and *in vitro* biological perspectives

Paranthaman Vijayan<sup>1</sup> | Periasamy Viswanathamurthi<sup>1</sup> | Paramasivam Sugumar<sup>2</sup> |  
Mondikalipudur Nanjappagounder Ponnuswamy<sup>2</sup> | Jan Grzegorz Malecki<sup>3</sup> |  
Krishnaswamy Velmurugan<sup>4</sup> | Raju Nandhakumar<sup>4</sup> | Manickam  
Dakshinamoorthi Balakumaran<sup>5</sup> | Pudupalayam Thangavelu Kalaichelvan<sup>5</sup>

<sup>1</sup>Department of Chemistry, Periyar University, Salem 636 011, India

<sup>2</sup>Centre of Advanced Studies in Crystallography and Biophysics, University of Madras, Guindy Campus, Chennai 600 025, India

<sup>3</sup>Department of Crystallography, Silesian University, Szkolna 9, 40-006 Katowice, Poland

<sup>4</sup>Department of Chemistry, Karunya University, Karunya Nagar, Coimbatore 641 114, India

<sup>5</sup>Centre for Advanced Studies in Botany, School of Life Sciences, University of Madras, Guindy Campus, Chennai 600 025, Tamil Nadu, India

## Correspondence

Periasamy Viswanathamurthi, Department of Chemistry, Periyar University, Salem – 636 011, India.

Email: viswanathamurthi72@gmail.com

*N,N*-[(diethylamino)(thiocarbonyl)]-substituted benzimidine ligands have been synthesized from the reaction of *N,N*-[(diethylamino)(thiocarbonyl)]benzimidoyl chloride with functionalized amines such as 2-aminophenol and 2-picolyamine. The reaction of *N,N*-[(diethylamino)(thiocarbonyl)]-2-hydroxyphenylbenzimidine (**H<sub>2</sub>L<sub>1</sub>**) with ruthenium(II) precursor [RuHCl(CO)(PPh<sub>3</sub>)<sub>3</sub>] afforded complex **1** of the type [Ru(L<sub>1</sub>)(CO)(PPh<sub>3</sub>)<sub>2</sub>] in which the ligand coordinated in tridentate ONS mode. The reaction of **H<sub>2</sub>L<sub>1</sub>** with copper precursor [Cu(CH<sub>3</sub>COO)(PPh<sub>3</sub>)<sub>2</sub>] induced C=N bond cleavage of the ligand and afforded complex **3** of the type [Cu(1,1-DT)(Cl)(PPh<sub>3</sub>)<sub>2</sub>] (1,1-DT = 1,1-diethylthiourea) in which the ligand coordinated in a monodentate fashion. The ligand *N,N*-[(diethylamino)(thiocarbonyl)]-2-picolybenzimidine (**HL<sub>2</sub>**) reacted with ruthenium(II) and copper(I) precursors to form complex **2** of the type [Ru(1,1-DT)(Cl<sub>2</sub>)(CO)(PPh<sub>3</sub>)<sub>2</sub>] and complex **3**, respectively, in which the ligand underwent C=N cleavage and coordinated in a monodentate fashion via C=S group. In complexes **1** and **2**, the two triphenylphosphine co-ligands coordinated in *trans* position whereas, in complex **3**, the two triphenylphosphine co-ligands coordinated in *cis* position. All the compounds were characterized using infrared, UV–visible, (<sup>1</sup>H, <sup>13</sup>C, <sup>31</sup>P) NMR, ESI-MS and elemental analyses. The molecular structures of ligand **H<sub>2</sub>L<sub>1</sub>** and complexes **1–3** were determined using X-ray crystallography, which confirmed the coordination mode of the ligands with metals. The crystal structure of complexes **1** and **2** revealed a distorted octahedral geometry around the ruthenium ion and the structure of complex **3** indicated a tetrahedral geometry around the copper ion. With the X-ray structures, density functional theory computations were carried out to determine the electronic structure of the compounds. The interactions of complexes **1–3** with calf thymus DNA and bovine serum albumin protein were investigated using UV–visible and fluorescence spectroscopic and viscometric methods. Catecholase- and phosphatase-like activities promoted by complexes **1–3** under physiological conditions have been studied. *In vitro* anticancer activities have been demonstrated by MTT assay, acridine orange/ethidium bromide and diamidino-2-phenylindole staining against various cancerous cell lines.

## KEYWORDS

anticancer activities *in vitro*, DFT, DNA/BSA binding, enzyme catalysis, ruthenium (II)/copper(I) complex

## 1 | INTRODUCTION

In recent years, there has been a surge in the development of thiourea-based ligands that support highly reactive transition metal complexes. *N,N*-(dialkylamino) (thiocarbonyl) benzamidine has been observed as a diverse selection of multifunctional thiourea scaffolds that can support metal ions by providing a wide variety of different steric and electronic environments.<sup>[1–3]</sup> The benzamidine ligands can readily be prepared by the simple reaction between the corresponding benzimidoyl chlorides and functionalized primary amines.<sup>[4]</sup> Due to the simultaneous presence of O, N, S electron donors, the substituted benzamidine ligands exhibit diverse coordination modes (Scheme 1) and form stable complexes with a large number of transition metal ions.<sup>[5,6]</sup>

Among these, the dibasic tridentate (ONS, SSS, SOS, SNS or SNN) mode of coordination is very common and many examples have been reported previously.<sup>[2,7]</sup> But coordination of benzamidine ligands to the metal ion in monodentate fashion through the sulfur atom is rare. However, recently there have been a few reports of ruthenium(II) arene complexes with thiourea ligands forming a six-membered ring, in which ruthenium is coordinated by monodentate sulfur atom without any internal cleavage in ligands due to intramolecular hydrogen bonding between the thiourea N–H and the amidic oxygen donor atom.<sup>[8,9]</sup> In the present paper, hydrolytic cleavage via C=N bond in the benzamidine ligands during the formation of new ruthenium(II) and copper(I) complexes is reported.

Cisplatin, carboplatin and oxaliplatin are proven anticancer drugs used worldwide for the treatment of a range of cancers. Nevertheless, there is limited effectiveness due to severe side effects and acquired resistance due to prolonged treatment which have spurred investigators to find alternative metal-based drugs.<sup>[10]</sup> Among them, ruthenium(II)/copper(I) incorporating benzamidine ligands have attracted much attention due to their interesting biological properties, particularly

their binding capability with DNA/nuclear proteins. Many important applications of these complexes require that they can bind to DNA via an intercalative mode that could induce cellular degradation. The planarity of the ligand and the presence of aromatic systems could favour the intercalation. Moreover, the binding of drugs to serum albumin *in vitro*, considered as a model in protein chemistry to study the binding behaviour of proteins, has been an interesting research field in bioinorganic chemistry. The binding of protein folded drugs (metal complexes) has made an important contribution to the stabilization of extracellular fluid volume by contributing to oncotic pressure (known also as colloid osmotic pressure), and assistance in the transport and distribution of body fluids between blood vessels and body tissues.<sup>[11,12]</sup> Therefore, the development of anticancer agents targeting both DNA and proteins has been much in demand.

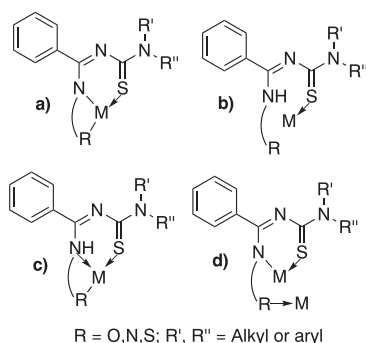
A number of catalysts having bio-mimicking activity for various enzymes have been designed by chemists. Such artificial enzymes have the same catalytic function but they are more stable and structurally less complex than enzymes. In particular, biochemically important enzymatic processes like catalytic oxidation of 3,5-di-*tert*-butylcatechol to quinone (catecholase activity) and hydrolytic reactions, i.e. hydrolysis of phosphodiester bond (phosphodiester cleavage), are of considerable importance.<sup>[13]</sup> Synthetic enzyme models are helpful in understanding the mechanistic aspects of enzyme action. Studies of metal complexes which mimic the activities of catecholase and phosphatase are very useful and promising for the development of bioinspired environmentally friendly catalysts.

Based on the above considerations, in the work reported here, the reactions between *N,N*-[(diethylamino) (thiocarbonyl)]-substituted benzamidine ligands with ruthenium(II)/copper(I) precursors were carried out and the coordination flexibility of ligands was studied (Schemes 2 and 3). Moreover, complexes 1–3 were also investigated using density functional theory (DFT) calculation, and their DNA/bovine serum albumin (BSA) binding, enzyme kineticocatalytic properties and *in vitro* anticancer activities studied.

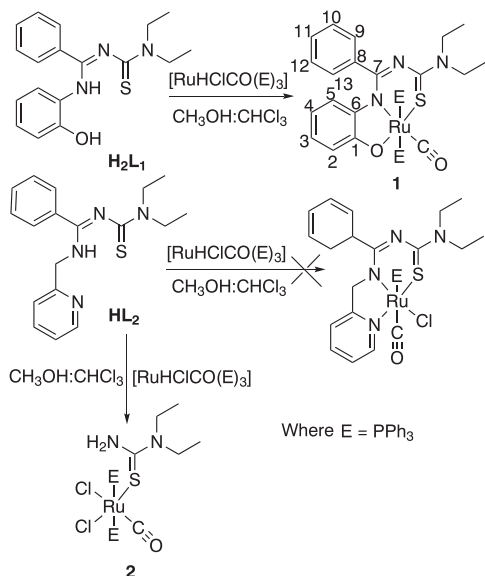
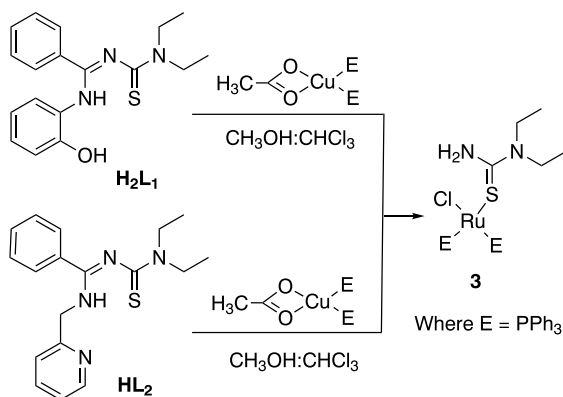
## 2 | EXPERIMENTAL

## 2.1 | Materials

All chemicals used in this study were of reagent grade and used without further purification. Synthetic manipulations were routinely performed under oxygen atmosphere. Doubly distilled water was used to prepare buffers. Calf thymus DNA (CT-



SCHEME 1 Diverse coordination modes of benzamidine ligands

SCHEME 2 Synthetic route of complexes **1** and **2**SCHEME 3 Synthetic route of complex **3**

DNA), BSA and 4-nitrophenyl phosphate disodium salt hexahydrate (4-NPP) were obtained from Genei, Bangalore and Himedia, India, respectively. Ethidium bromide (EB), 3,5-di-*tert*-butylcatechol (3,5-DTBC) and tris(hydroxymethyl) aminomethane were purchased from Sigma-Aldrich and used as received.

## 2.2 | General methods

Elemental analyses (C, H, N and S) were carried out with a Vario EL III CHNS analyser. Infrared (IR) spectra were recorded as KBr pellets using a PerkinElmer FT-IR spectrophotometer in the range 400–4000  $\text{cm}^{-1}$ . ( $^1\text{H}$ ,  $^{13}\text{C}$ ) NMR spectra were measured with a Bruker Ultra Shield at 300 MHz using DMSO- $d_6$  or  $\text{CDCl}_3$  as solvent and tetramethylsilane as an internal reference.  $^{31}\text{P}$  NMR spectra were measured with a Bruker Ultra Shield at 300 MHz using DMSO- $d_6$  or  $\text{CDCl}_3$  as solvent and *o*-phosphoric acid as an external standard. Mass spectra for the complexes were obtained with an advanced Q-TOF micro<sup>TM</sup> mass spectrometer using an electrospray ionization probe. All mass spectral data are given in the form:  $m/z$ , assignment. Electronic

spectra were obtained with a JASCO V-570 spectrophotometer. Geometry optimization with the DFT method was performed using the B3LYP (LANL2DZ/6-311G) package. Fluorescence spectral data were obtained with a JASCO FP-8200 fluorescence spectrophotometer at room temperature. Single-crystal X-ray diffraction data collections were carried out at 293(2)–296(2) K with a Bruker Apex-II CCD area detector (for **H<sub>2</sub>L<sub>1</sub>**, **1** and **2**) and Gemini A Ultra (for **3**). The melting points were checked on a Technico micro heating apparatus and are uncorrected. Stock solutions of compounds ( $1.0 \times 10^{-3}$  M in DMSO) were stored at 4 °C and required concentrations were prepared for all experiments. All the stock solutions were used after no more than four days. Solutions of compounds were freshly prepared 1 h prior to biochemical evaluation. Data were expressed as the mean  $\pm$  the standard deviation from three independent experiments.

## 2.3 | Synthesis of $[\text{Ru}(\text{L}_1)(\text{CO})(\text{PPh}_3)_2]$ (**1**)

A solution of **H<sub>2</sub>L<sub>1</sub>** (0.1 mmol) in 20 ml of MeOH– $\text{CHCl}_3$  (1:1 v/v) was added dropwise to a boiling solution of  $[\text{RuHCl}(\text{CO})(\text{PPh}_3)_3]$  (0.100 g, 0.1 mmol) in a MeOH– $\text{CHCl}_3$  solvent mixture (1:1 v/v) (20 ml). The mixture was gently heated under reflux for 12 h, which resulted in a rapid change of colour from light yellow to maroon. The reaction was monitored by TLC using a silica gel on aluminium sheets with a 90/10 mixture of petroleum ether–ethyl acetate as the mobile phase. After completion of the reaction, the resulting solution was filtered and the filtrate was left standing for slow evaporation of the solvent. After three days reddish-brown coloured small size crystals suitable for X-ray diffraction were obtained. Yield 85%; brown. Micro analytical data for  $\text{C}_{55}\text{H}_{49}\text{N}_3\text{O}_2\text{P}_2\text{RuS}$  required (%): C, 67.47; H, 5.04; N, 4.29; S, 3.28. Found (%): C, 67.32; H, 5.01; N, 4.11; S, 3.09. IR (KBr pellet,  $\text{cm}^{-1}$ ): 1527 (C=N), 820 (C=S), 1951 (C  $\equiv$  O).  $^1\text{H}$  NMR (DMSO- $d_6$ , ppm): 1.15 (t,  $J = 7.0$  Hz, 3H,  $\text{CH}_3$ ), 1.19 (t,  $J = 7.0$  Hz, 3H,  $\text{CH}_3$ ), 3.64 (q,  $J = 7.0$  Hz, 2H,  $\text{CH}_2$ ), 3.81 (q,  $J = 7.0$  Hz, 2H,  $\text{CH}_2$ ), 6.65 (d,  $J = 7.2$  Hz, 1H,  $\text{H}_2$ ), 6.67 (d,  $J = 7.2$  Hz, 1H,  $\text{H}_5$ ), 6.72 (dd,  $J_{(4-3)} = 7.2$  Hz,  $J_{(4-5)} = 7.2$  Hz 1H,  $\text{H}_4$ ), 6.81 (dd,  $J_{(3-2)} = 7.2$  Hz,  $J_{(3-4)} = 7.2$  Hz 1H,  $\text{H}_3$ ), 6.85 (dd,  $J_{(10-9)} = 7.4$  Hz,  $J_{(10-11)} = 7.4$  Hz, 1H,  $\text{H}_{10}$ ), 6.85 (dd,  $J_{(12-13)} = 7.4$  Hz,  $J_{(12-11)} = 7.4$  Hz, 1H,  $\text{H}_{12}$ ), 6.89 (s, 1H,  $\text{H}_{11}$ ), 7.25 (d,  $J = 7.7$  Hz, 2H,  $\text{H}_{9,13}$ ), 7.41–7.61 (m,  $\text{PPh}_3$ ).  $^{13}\text{C}$  NMR ( $\text{CDCl}_3$ , ppm): 203.01 (C  $\equiv$  O), 169.19 (C=S), 165.85 (C–O,  $\text{C}_1$ ), 158.08 (C=N,  $\text{C}_7$ ), 141.99 (C–N,  $\text{C}_7$ ), 132.65 (Ar  $\text{C}_6$ ), 132.30 (Ar  $\text{C}_2$ ), 132.15 (Ar  $\text{C}_5$ ), 132.10 (Ar  $\text{C}_4$ ), 132.04 (Ar  $\text{C}_3$ ), 131.89 (Ar  $\text{C}_8$ ), 131.75 (Ar  $\text{C}_9$ ), 131.60 (Ar  $\text{C}_{13}$ ), 131.44 (Ar  $\text{C}_{10}$ ), 126.42 (Ar  $\text{C}_{12}$ ), 126.35 (Ar  $\text{C}_{11}$ ), 126.10–117.62 ( $\text{PPh}_3$ ), 13.21, 13.31 ( $\text{CH}_3$ , C), 47.61, 48.74 ( $\text{CH}_2$ , C).  $^{31}\text{P}$  NMR (DMSO- $d_6$ , ppm): 36.98. UV–visible ( $\text{CHCl}_3$ ,  $\lambda_{\text{max}}$  (nm) ( $\epsilon$ ,  $\text{dm}^3 \text{mol}^{-1} \text{cm}^{-1}$ ): 238 (46 400), 268 (24 800), 307 (16 740), 474 (6580). ESI-MS (calcd, found,  $m/z$ ): 979.08,

980.4 (M)<sup>+</sup>. Single crystals suitable for X-ray determination were grown by slow evaporation of methanol–chloroform (1:1 v/v) solution of **1** at room temperature.

## 2.4 | Synthesis of [Ru(1,1-DT)(Cl<sub>2</sub>)(CO)(PPh<sub>3</sub>)<sub>2</sub>] (**2**)

Complex **2** was prepared using the above procedure by reacting a suspension of [RuHCl(CO)(PPh<sub>3</sub>)<sub>3</sub>] with **HL**<sub>2</sub>. Yield 76%; yellow. Micro analytical data for C<sub>42</sub>H<sub>42</sub>Cl<sub>2</sub>N<sub>2</sub>O<sub>2</sub>P<sub>2</sub>RuS required (%): C, 58.88; H, 4.94; N, 3.27; S, 3.74. Found (%): C, 58.54; H, 4.79; N, 3.04; S, 3.65. IR (KBr pellet, cm<sup>-1</sup>): 3381 (NH<sub>2</sub>), 829 (C=S), 1952 (C≡O). <sup>1</sup>H NMR (CDCl<sub>3</sub>, ppm): 1.22 (t, *J* = 7.2 Hz, 3H, CH<sub>3</sub>), 1.26 (t, *J* = 7.2 Hz, 3H, CH<sub>3</sub>), 3.85 (q, *J* = 7.2 Hz, 2H, CH<sub>2</sub>), 3.94 (q, *J* = 7.2 Hz, 2H, CH<sub>2</sub>), 7.19–7.89 (m, PPh<sub>3</sub>), 8.17 (s, NH<sub>2</sub>). <sup>13</sup>C NMR (CDCl<sub>3</sub>, ppm): 204.12 (C≡O), 177.69 (C=S), 140.66 (C–N), 118.41–125.44 (m, PPh<sub>3</sub>) 14.42, 14.65 (CH<sub>3</sub>), 46.50, 47.71 (CH<sub>2</sub>). <sup>31</sup>P NMR (DMSO-*d*<sub>6</sub>, ppm): 34.83. UV–vis (CHCl<sub>3</sub>, λ<sub>max</sub> (nm) (*ε*, dm<sup>3</sup> mol<sup>-1</sup> cm<sup>-1</sup>)): 239 (45 400), 273 (26 800), 330 (11 200), 420 (1800). ESI-MS (calcd, found, *m/z*): 856.78, 822.3 (M – Cl)<sup>+</sup>. Single crystals suitable for X-ray determination were grown by slow evaporation of methanol–chloroform (1:1 v/v) solution of **2** at room temperature.

## 2.5 | Synthesis of [Cu(1,1-DT)(Cl)(PPh<sub>3</sub>)<sub>2</sub>] (**3**)

Complex **3** was prepared by a procedure similar to that used for complex **1** by reacting equimolar quantity of the ligands (**H**<sub>2</sub>**L**<sub>1</sub> or **HL**<sub>2</sub>) (0.1 mmol) in 10 ml of methanol and a suspension of [Cu(CH<sub>3</sub>COO)(PPh<sub>3</sub>)<sub>2</sub>] (0.1 mmol) in 10 ml of chloroform. After completion of the reaction, the resulting solution was filtered and the filtrate was left standing for the slow evaporation of the solvent. After four days orange coloured crystals suitable for X-ray diffraction were obtained. Yield 60%; orange. Micro analytical data for C<sub>41</sub>H<sub>42</sub>ClCuN<sub>2</sub>P<sub>2</sub>S required (%): C, 65.15; H, 5.60; N, 3.71; S, 4.24. Found (%): C, 65.01; H, 5.51; N, 3.61; S, 4.11. IR (KBr pellet, cm<sup>-1</sup>): 3379 (NH<sub>2</sub>), 814 (C=S). <sup>1</sup>H NMR (CDCl<sub>3</sub>, ppm): 1.37 (t, *J* = 7.2 Hz, 3H, CH<sub>3</sub>), 1.62 (t, *J* = 7.2 Hz, 3H, CH<sub>3</sub>), 3.68 (q, *J* = 7.2 Hz, 2H, CH<sub>2</sub>), 3.52 (q, *J* = 7.2 Hz, 2H, CH<sub>2</sub>), 6.43–7.65 (m, PPh<sub>3</sub>), 8.21 (s, NH<sub>2</sub>). <sup>13</sup>C NMR (CDCl<sub>3</sub>, ppm): 171.44 (C=S), 140.66 (C–N), 121.41–131.53 (m, PPh<sub>3</sub>), 13.91, 14.09 (CH<sub>3</sub>), 48.17, 49.61 (CH<sub>2</sub>). <sup>31</sup>P NMR (DMSO-*d*<sub>6</sub>, ppm): –3.80. UV–visible (CHCl<sub>3</sub>, λ<sub>max</sub> (nm) (*ε*, dm<sup>3</sup> mol<sup>-1</sup> cm<sup>-1</sup>)): 238 (45 800), 263 (35 200), 333 (19 400). ESI-MS (calcd, found, *m/z*): 755.8, 721.3 (M – Cl)<sup>+</sup>. Single crystals suitable for X-ray determination were grown by slow evaporation of methanol–chloroform (1:1 v/v) solution of **3** at room temperature.

## 2.6 | X-ray structure determination

Crystals of **H**<sub>2</sub>**L**<sub>1</sub> and **1–3** suitable for single-crystal X-ray analysis were obtained from slow evaporation of methanol–chloroform solutions. The crystal data collections were

performed with a Bruker SMART APEX 2 at 293(2)–296 (2) K and a Gemini Ultra Oxford Diffraction automatic diffractometer equipped with a CCD detector. Suitable single crystals of compounds were mounted on a glass fibre with epoxy cement. The crystals were cut into a fitting size (less than collimator cross-sectional diameter). The X-ray radiation employed was generated from Mo sealed X-ray tube (Kα, λ = 0.71073 Å) fitted with a graphite monochromator for all compounds. The data were corrected for Lorentz and polarization effects with the SMART suite of programs and for absorption effects with SADABS<sup>[14]</sup> and SCALE3 ABSPACK (CrysAlis RED, Oxford Diffraction Ltd, Version 1.171.29.2) scaling algorithm. A data collection strategy using ω and φ scans at 0.5° scan technique yielded full hemispherical data with excellent intensity statistics. Structure solutions and refinements were done using the programs SHELXS-97/14. The structures were solved by direct methods to locate the heavy atoms, followed by difference maps for the light non-hydrogen atoms. Anisotropic thermal parameters were refined for the rest of the non-hydrogen atoms. Hydrogen atoms were placed geometrically and refined isotropically. Details of the data collection and refinement are gathered in Table 1 and important bond lengths and angles for the compounds are summarized in Table 2.

## 2.7 | Theoretical calculation (DFT)

The calculations were carried out using the Gaussian 09 program.<sup>[15]</sup> The DFT/B3LYP method was used for the geometry optimization and electronic structure determination. The calculations were performed using the DZVP basis set on ruthenium atom and 6-311 g (d, p) basis set was used to describe the copper atom. The PCM solvent model was used to calculate the electronic structures with trichloromethane as the solvent. GaussSum 3.0 was used to calculate group (ligands and metal centre) contribution to the molecular orbitals.<sup>[16]</sup> The molecular orbital plots were generated using the Chemcraft program package (<http://www.chemcraftprog.com>).

## 2.8 | DNA binding studies

### 2.8.1 | Emissive titration

Fluorescence spectra titrations were performed at room temperature in 95% Tris–HCl/NaCl buffer (5 mM Tris–HCl/50 mM NaCl buffer, pH = 7.2) to investigate the binding affinity between CT-DNA and complexes **1–3**. Mixing of such solutions with the aqueous buffer DNA solutions used in the studies never exceeded 5% (v/v) DMSO in the final solution, which was needed due to low aqueous solubility of most compounds. The CT-DNA concentration per nucleotide was determined by fluorescence spectrometry using the complex excitation wavelength. During titration, an equal quantity of CT-DNA was added to both the complex solution and reference solution to eliminate the intensity of CT-DNA

TABLE 1 Crystal data and structure refinement for  $H_2L_1$  and complexes 1–3

	$H_2L_1$			1	2	3
Empirical formula	$C_{18}H_{21}N_3O_5$	$C_{35}H_{49}N_5O_2P_2RuS$	$C_{35}H_{49}N_5O_2P_2RuS$	$C_{42}H_{41}Cl_3N_2OP_2RuS$	$C_{41}H_{42}ClCuN_2P_2S$	
Formula weight	327.44	979.04	979.04	855.74	755.75	
Temperature (K)	293(2)	293(2)	293(2)	296(2)	295(2)	
Wavelength (Å)	0.71073	0.71073	0.71073	0.71073	0.71073	
Crystal system	Triclinic	Orthorhombic	Orthorhombic	Monoclinic	Triclinic	
Space group	P-1	P212121	P212121	P2 <sub>1</sub> /c	P-1	
Unit cell dimensions						
<i>a</i> (Å)	7.947(5)	11.2101(8)	11.2101(8)	12.1056(10)	10.6722(4)	
<i>b</i> (Å)	13.065(5)	19.2499(6)	19.2499(6)	19.1325(15)	13.3220(4)	
<i>c</i> (Å)	18.136(5)	21.1428(4)	21.1428(4)	17.8135(15)	14.9460(5)	
$\alpha$ (°)	70.513(5)	90	90	90	79.311(3)	
$\beta$ (°)	77.564(5)	90	90	107.163(2)	69.506(3)	
$\gamma$ (°)	74.419(5)	90	90	90	70.796(3)	
Volume (Å <sup>3</sup> )	1693.4(13)	4562.5(4)	4562.5(4)	3942.1(6)	1873.75(12)	
Z	4	4	4	4	2	
Density (calcd) Mg M <sup>-3</sup>	1.284	1.425	1.425	1.442	1.340	
Absorption coefficient (mm <sup>-1</sup> )	0.199	0.507	0.507	0.703	0.827	
<i>F</i> (000)	696	2024	2024	1756	788	
Theta range for data collection (°)	1.20 to 26.38	1.43 to 28.42	1.43 to 28.42	1.60 to 25.00	3.452 to 25.375	
Index ranges	-9 ≤ <i>h</i> ≤ 9 -16 ≤ <i>k</i> ≤ 16 -22 ≤ <i>l</i> ≤ 22	-13 ≤ <i>h</i> ≤ 14 -15 ≤ <i>k</i> ≤ 24 -22 ≤ <i>l</i> ≤ 28	-13 ≤ <i>h</i> ≤ 14 -15 ≤ <i>k</i> ≤ 24 -22 ≤ <i>l</i> ≤ 28	-14 ≤ <i>h</i> ≤ 14 -22 ≤ <i>k</i> ≤ 22 -21 ≤ <i>l</i> ≤ 21	-14 ≤ <i>h</i> ≤ 13 -18 ≤ <i>k</i> ≤ 16 -19 ≤ <i>l</i> ≤ 20	
Reflections collected	24 570	22 810	22 810	106 795	24 350	
Independent reflections	6902 [ <i>R</i> (int) = 0.0670]	10999 [ <i>R</i> (int) = 0.1665]	10999 [ <i>R</i> (int) = 0.1665]	6941 [ <i>R</i> (int) = 0.0939]	9068 [ <i>R</i> (int) = 0.0609]	
Data/restraints/parameters	6902/0/419	10999/0/579	10999/0/579	6941/61/487	9068/0/435	
Goodness-of-fit on <i>F</i> <sup>2</sup>	1.055	0.929	0.929	1.289	1.034	
Final <i>R</i> indices [ <i>I</i> > 2σ( <i>I</i> )]	<i>R</i> 1 = 0.1244, <i>wR</i> 2 = 0.1244	<i>R</i> 1 = 0.0685, <i>wR</i> 2 = 0.1448	<i>R</i> 1 = 0.0685, <i>wR</i> 2 = 0.1448	<i>R</i> 1 = 0.0534, <i>wR</i> 2 = 0.1131	<i>R</i> 1 = 0.0386, <i>wR</i> 2 = 0.0834	
<i>R</i> indices (all data)	<i>R</i> 1 = 0.0670, <i>wR</i> 2 = 0.1395	<i>R</i> 1 = 0.1665, <i>wR</i> 2 = 0.1895	<i>R</i> 1 = 0.1665, <i>wR</i> 2 = 0.1895	<i>R</i> 1 = 0.0939, <i>wR</i> 2 = 0.1549	<i>R</i> 1 = 0.0609, <i>wR</i> 2 = 0.0930	

TABLE 2 Selected bond lengths (Å) and bond angles (°) for  $H_2L_1$  and complexes 1–3 with the optimized geometrical values

$H_2L_1$	X-ray	DFT	1	X-ray	DFT	2	X-ray	DFT	3	X-ray	DFT	X-ray	DFT
C(14)–S(1)	1.695(2)	1.751	C(55)–Ru(1)	1.863(10)	1.874	C(37)–Ru(1)	1.826(7)	1.850	C(1)–Cu(1)	2.391(6)	2.391	2.391(6)	2.391
C(32)–S(2)	1.693(2)	1.734	N(1)–Ru(1)	2.166(7)	2.151	P(2)–Ru(1)	2.3964(17)	2.524	S(1)–Cu(1)	2.3684(6)	2.368	2.3684(6)	2.368
C(14)–N(2)	1.373(2)	1.375	O(2)–Ru(1)	2.161(5)	2.099	P(1)–Ru(1)	2.4025(16)	2.523	P(1)–Cu(1)	2.2986(5)	2.299	2.2986(5)	2.299
C(14)–N(3)	1.332(2)	1.361	P(2)–Ru(1)	2.4023(19)	2.516	S(2)–Ru(1)	2.4096(16)	2.574	P(2)–Cu(1)	2.3094(6)	2.309	2.3094(6)	2.309
C(32)–N(5)	1.376(2)	1.401	P(4)–Ru(1)	2.403(2)	2.547	Cl(1)–Ru(1)	2.4432(16)	2.505					
C(32)–N(6)	1.333(3)	1.359	S(1)–Ru(1)	2.345(2)	2.480	Cl(2)–Ru(1)	2.4750(16)	2.585	S(1)–Cu(1)–Cl(1)	111.76(2)	111.8	111.76(2)	111.8
C(7)–N(1)	1.354(2)	1.374							P(1)–Cu(1)–Cl(1)	102.86(2)	102.9	102.86(2)	102.9
C(6)–N(1)	1.408(2)	1.408	C(55)–Ru(1)–O(2)	94.3(3)	95.5	P(2)–Ru(1)–S(2)	93.35(6)	88.6	P(1)–Cu(1)–S(1)	104.82(2)	104.8	104.82(2)	104.8
C(31)–N(4)	1.352(2)	1.369	O(2)–Ru(1)–N(1)	77.5(2)	80.0	P(1)–Ru(1)–S(2)	84.84(6)	96.6	P(1)–Cu(1)–P(2)	121.64(2)	121.6	121.64(2)	121.6
C(24)–N(4)	1.410(2)	1.430	N(1)–Ru(1)–P(4)	94.1(2)	93.4	C(37)–Ru(1)–Cl(1)	86.4(2)	86.7	P(2)–Cu(1)–Cl(1)	104.72(2)	104.7	104.72(2)	104.7
C(1)–O(1)	1.358(3)	1.404	S(1)–Ru(1)–P(4)	91.36(8)	86.8	P(2)–Ru(1)–Cl(1)	93.88(6)	87.5	P(2)–Cu(1)–S(1)	110.80(2)	110.8	110.80(2)	110.8
C(19)–O(2)	1.363(3)	1.380	C(55)–Ru(1)–S(1)	93.7(3)	90.1	P(1)–Ru(1)–Cl(1)	87.87(6)	87.6					
			C(55)–Ru(1)–P(2)	90.7(3)	89.6	S(2)–Ru(1)–Cl(1)	167.54(6)	169.4					
S(1)–C(14)–N(2)	120.20(14)	120.9	O(2)–Ru(1)–S(1)	171.93(16)	174.1	C(37)–Ru(1)–Cl(2)	173.9(2)	178.9					
S(1)–C(14)–N(3)	123.49(14)	123.5	C(55)–Ru(1)–N(1)	171.7(3)	175.5	P(2)–Ru(1)–Cl(2)	87.60(6)	89.4					
S(2)–C(32)–N(5)	119.93(16)	122.0	P(2)–Ru(1)–P(4)	175.92(8)	175.8	P(1)–Ru(1)–Cl(2)	92.94(6)	87.3					
S(2)–C(32)–N(6)	123.73(15)	123.8	C(50)–S(1)–Ru(1)	104.6(4)	103.6	S(2)–Ru(1)–Cl(2)	101.73(6)	96.7					
C(6)–C(1)–O(1)	117.95(17)	115.0	O(1)–C(55)–Ru(1)	177.8(9)	179.0	Cl(1)–Ru(1)–Cl(2)	88.71(6)	93.0					
C(24)–C(19)–O(2)	117.88(18)	123.4	N(1)–Ru(1)–S(1)	94.50(19)	94.3	C(40)–S(2)–Ru(1)	118.2(2)	118.3					

itself and Tris-HCl/NaCl buffer was subtracted through baseline correction. Emissive titration experiments were performed with a fixed concentration of complexes **1–3** (25  $\mu\text{M}$ ). While gradually increasing the concentration (0–10  $\mu\text{M}$ ) of DNA, the emission intensities were recorded for complexes in the range 350–650 nm. Titrations were manually done by a micropipette for the addition of CT-DNA.

### 2.8.2 | EB displacement assay

The relative binding propensity of complexes to CT-DNA was determined with an EB-bound CT-DNA solution in Tris-HCl/NaCl buffer (5 mM Tris-HCl/50 mM NaCl buffer, pH = 7.2). The fluorescence spectra were recorded at excitation wavelength of 510 nm for an emission range of 604 nm. In the fluorescence quenching spectra, the reduction in emission intensity measured the binding mode of complexes to CT-DNA. The addition of increasing amounts of the complexes to the DNA-EB adduct quenched the fluorescence. Before the emission spectra were recorded, CT-DNA was pretreated with EB in the ratio [DNA]/[EB] = 1 for 30 min at room temperature in order to fully react. Then the titration compounds were added to this mixture of EB-DNA and the changes in the fluorescence intensity were recorded.

### 2.8.3 | Viscosity experiment.

Viscosity measurements were carried out using an Ubbelodhe viscometer maintained at a constant temperature of 30.0  $^{\circ}\text{C}$  ( $\pm 0.1$   $^{\circ}\text{C}$ ) in a thermostatic bath. The flow time was measured three times, after 5 min of incubation with each addition of the complexes **1–3** and the average flow time was taken for calculation of relative viscosity. Relative viscosities for CT-DNA in the presence and absence of the complexes were calculated from the relation  $\eta = (t - t_0)/t_0$ , where  $t$  is the observed flow time of DNA-containing solution and  $t_0$  is the flow time of Tris-HCl/NaCl buffer alone. Data were presented as  $(\eta/\eta_0)^{1/3}$  versus binding ratio ( $r = [\text{compounds}]/[\text{DNA}] = 0.0\text{--}0.1$ ), where  $\eta$  is the viscosity of CT-DNA in the presence of the compound and  $\eta_0$  is the viscosity of CT-DNA alone.

## 2.9 | Protein binding studies

The binding mode of complexes **1–3** with BSA was investigated using fluorescence spectra at room temperature with an excitation wavelength for BSA at 280 nm and monitoring the emission at 344 nm by keeping the concentration of BSA constant (1  $\mu\text{M}$ ) while increasing the complex concentration (0–50  $\mu\text{M}$ ) regularly. The excitation and emission slit widths (each 5 nm) remained constant for all the experiments. A scan rate of 200 nm  $\text{min}^{-1}$  was used. In addition, absorption titration experiments were carried out by keeping the concentration of the complexes (20  $\mu\text{M}$ ) and BSA (1  $\mu\text{M}$ ) as constant. Furthermore, the type of quenching mechanism of complexes was determined from UV-visible absorption spectra in the range 200–600 nm.

## 2.10 | Enzyme kinetic studies

### 2.10.1 | Catechol oxidation

These kinetic experiments were carried out using fluorescence quenching spectra under pseudo-first-order conditions.<sup>[17]</sup> Complexes **1–3** were preferred as representative catalysts to study the catalytic oxidation of catechol. The emission intensity of 3,5-DTBC at  $\lambda_{\text{emis}} = 435$  nm ( $\lambda_{\text{ex}} = 401$  nm) was monitored using selected compounds. Complexes **1–3** ( $1 \times 10^{-4}$  M) in DMF were added to 100 equivalents of  $1 \times 10^{-3}$  M solutions of 3,5-DTBC under aerobic conditions. Emissive intensity of the resultant reaction mixture was plotted with respect to wavelength at a regular interval of 15 min using a fluorescence spectrophotometer in the range 410–700 nm. The dependence of the rate on substrate concentration and different kinetic parameters were obtained by treatment of complexes with 3,5-DTBC and monitoring the increase in emission intensity at 435 nm (the peak corresponding to the quinone band maxima) as a function of time.

### 2.10.2 | Phosphate ester hydrolysis

The hydrolysis of 4-NPP was determined using fluorescence quenching spectroscopy. Its hydrolytic tendency was measurable spectrophotometrically by monitoring the time evolution of *p*-nitrophenolate in DMF through a wavelength scan from 410 to 700 nm over 2 h. The emission intensity of 4-NPP at 485 nm ( $\lambda_{\text{ex}} = 401$  nm) was monitored using complexes **1–3**. The hydrolase activity involved the preparation of stock solutions of complexes ( $0.05 \times 10^{-3}$  M) and the substrate 4-NPP ( $1 \times 10^{-3}$  M), at higher concentrations in DMF. The dependence of the rate on various concentrations and different kinetic parameters were obtained by treatment of  $0.05 \times 10^{-3}$  M solution of complexes **1–3** with 40 equivalents of 4-NPP (the peak corresponding to the phenolate band maxima) as a function of time.

## 2.11 | In Vitro anticancer activities

### 2.11.1 | Cell culture

Human cervical cancer (HeLa), human hepatocellular carcinoma (HepG2) and human breast cancer (MCF-7) cell lines were obtained from the National Centre for Cell Sciences Repository, University of Pune, India. The normal Vero and cancer cells were maintained in a humidified atmosphere containing 5%  $\text{CO}_2$  at 37  $^{\circ}\text{C}$  in Dulbecco's modified Eagle's medium supplemented with 100 units of penicillin, 100  $\mu\text{g ml}^{-1}$  streptomycin and 10% foetal bovine serum. Briefly, normal Vero and cancer cells, HeLa, HepG2, MCF-7, were precultured in 96-well microtiter plates for 48 h under 5%  $\text{CO}_2$ . Complexes **1–3** were dissolved in 0.1% DMSO (the concentration of DMSO did not exceed 0.1% *v/v*) to obtain a solution of 1 mM each. The samples were then diluted to 100  $\mu\text{M}$  in phosphate-buffered saline (PBS) solution and filter-sterilized using a 0.22  $\mu\text{m}$  syringe filter. This

100  $\mu\text{M}$  solution in PBS was further used in cell cytotoxicity studies. The cells ( $1 \times 10^6$  cells  $\text{ml}^{-1}$  per well) were seeded in a 96-well plate. One day after seeding, the cells were treated with or without different concentrations of test complexes and re-incubated at 37  $^\circ\text{C}$  in a  $\text{CO}_2$  incubator for 24 h. After the incubation, the cells were visualized using an inverted Olympus microscope.

### 2.11.2 | Protocol for MTT assay

The MTT (3-(4,5-dimethylthiazol-2-yl)-2,5-diphenyltetrazolium bromide) assay is a quantitative, sensitive and reliable colorimetric technique generally used for assessing viability and proliferation of cells. Cell viability with complexes **1–3** against normal Vero and HeLa, HepG2 and MCF-7 cancer cell lines was determined by MTT assay.<sup>[18]</sup> Complexes **1–3** were added to micro-wells containing the cell culture at final concentrations in the range 10–100  $\mu\text{g ml}^{-1}$ . Then each well was loaded with 10  $\mu\text{l}$  of MTT solution (5  $\text{mg ml}^{-1}$  in PBS, pH = 7.4) for 4 h at 37  $^\circ\text{C}$ . The formed purple formazan crystals were dissolved in 200  $\mu\text{l}$  of DMSO and the cell viability was determined by calculating the absorbance of each well at 540 nm using a Bio-Rad ELISA plate reader.<sup>[19]</sup> All data were representative of three independent experiments, and the percentage of cell viability was calculated according to the following equation:

Inhibition rate (IR %) = [OD (control) – OD (drug-treated cells)/OD (control)]  $\times$  100.

<NI > The corresponding  $\text{IC}_{50}$  (concentration of drug that inhibits cell growth by 50%) value was determined by nonlinear regression analysis using Origin 6.0 software.

### 2.11.3 | Nuclear staining assay

Nuclear staining using acridine orange (AO)/EB and diamidino-2-phenylindole (DAPI) was measured by fluorescence microscopy according to the method previously described.<sup>[20]</sup> HeLa and HepG2 cancer cells ( $1 \times 10^6$  in number) were cultured in six-well plates at 37  $^\circ\text{C}$  in an incubator with fixed concentration of complexes **1–3** (50  $\mu\text{M}$ ) for 24 h. The cells were harvested and washed with ice-cold PBS and 40  $\mu\text{l}$  of AO/EB solution (1 part of 100  $\mu\text{g ml}^{-1}$  AO in PBS; 1 part of 100  $\mu\text{g ml}^{-1}$  EB in PBS) was added. After staining, the cells were washed with PBS twice, suspended in 200  $\mu\text{l}$  of PBS, and the nuclear morphology was observed under a fluorescence microscope in less than 20 min. For DAPI staining, the treated cells were fixed with 80% ethanol at room temperature for 30 min. The fixative was removed and the cells were washed three times with PBS, and then incubated with DAPI (1  $\mu\text{g ml}^{-1}$ ) for 45 min at room temperature in the dark. Both techniques were used to determine viable cells, early apoptotic cells with blebbing, and necrotic cells. The functions of dye have been reported beforehand.<sup>[31]</sup>

The HeLa and HepG2 cancer cells were mounted on slides, and the images were observed under a fluorescent microscope in green/blue filter with excitation at 350 nm and emission at 460 nm. At least 200 cells from each slide were

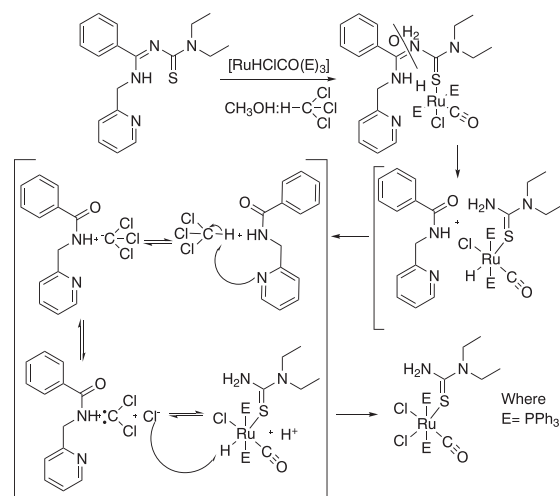
counted, and the percentage of apoptotic cells was calculated on the basis of cellular morphological features. The results were recorded as the mean of three independent experiments.

## 3 | RESULTS AND DISCUSSION

### 3.1 | Synthesis and characterization

Surprisingly little is known about the coordination behaviour of benzimidine ligands **H<sub>2</sub>L<sub>1</sub>** and **HL<sub>2</sub>**, which can be synthesized from the reactions of *N,N*-[(diethylamino) (thiocarbonyl)]benzimidoyl chloride with functionalized amines such as 2-aminophenol and 2-picolyamine in dry acetone.<sup>[21]</sup> In the presence of supporting base  $\text{NEt}_3$ , such reactions proceed quickly under mild conditions. The progress of the reaction can readily be checked by TLC on silica gel and is indicated by the formation of a colourless precipitate of  $\text{NEt}_3\cdot\text{HCl}$ , which is almost insoluble in acetone. We have relied on the use of the stable starting materials  $[\text{RuHCl}(\text{CO})(\text{PPh}_3)_3]$ <sup>[22]</sup> and  $[\text{Cu}(\text{CH}_3\text{COO})(\text{PPh}_3)_2]$ <sup>[23]</sup> for the synthesis of ruthenium(II)/copper(I) complexes. The reaction of **H<sub>2</sub>L<sub>1</sub>** with ruthenium(II) precursor  $[\text{RuHCl}(\text{CO})(\text{PPh}_3)_3]$  affords complex **1** of the type  $[\text{Ru}(\text{L}_1)(\text{CO})(\text{PPh}_3)_2]$  in which the ligand coordinates in tridentate ONS mode. While the reaction of **H<sub>2</sub>L<sub>1</sub>** with copper precursor  $[\text{Cu}(\text{CH}_3\text{COO})(\text{PPh}_3)_2]$  induces C=N bond cleavage of the ligand and affords complex **3** of the type  $[\text{Cu}(1,1\text{-DT})(\text{Cl})(\text{PPh}_3)_2]$  (1,1-DT = 1,1-diethylthiourea) in which the ligand coordinates in monodentate fashion.

The ligand **HL<sub>2</sub>** reacts with ruthenium(II) and copper(I) precursors to form complex **2** of the type  $[\text{Ru}(1,1\text{-DT})(\text{Cl}_2)(\text{CO})(\text{PPh}_3)_2]$  and complex **3**, respectively, in which the ligand undergoes C=N cleavage and coordinates in monodentate fashion via C=S group. The proposed mechanism for hydrolytic cleavage and solvent-assisted formation of complex **2** is shown in Scheme 4. The formation complex **3** follows the same mechanistic pathway. To the best of our



SCHEME 4 Proposed mechanism for the formation of complex **2**

knowledge, there are no other reports of hydrolytic cleavage in benzamidine ligands (Scheme 2) with ruthenium(II) and copper(I) complexes (**1–3**).

The new compounds are crystalline, non-hygroscopic solids, air-stable at room temperature, soluble in common organic solvents such as dichloromethane, chloroform, benzene, acetonitrile, ethanol, methanol, dimethylsulfoxide and dimethylformamide and insoluble in hexane, petroleum ether and diethyl ether. The analytical data for the compounds agree well with the proposed molecular formulae. These compounds have been systematically characterized using UV–visible, IR, NMR ( $^1\text{H}$ ,  $^{13}\text{C}$ ,  $^{31}\text{P}$ ) and ESI-MS spectral studies. In addition, the molecular structures of ligand **H<sub>2</sub>L<sub>1</sub>** and complexes **1–3** have been authenticated using single-crystal X-ray crystallography.

### 3.2 | Spectroscopic studies

The characteristic IR bands of ligands **H<sub>2</sub>L<sub>1</sub>** and **HL<sub>2</sub>** and their complexes **1–3** provide substantial information about metal–ligand bonding and all the bands are listed in Section 2. No attempt has been made to assign each individual band to a specific vibration. However, the IR spectra of ligands exhibit  $\nu_{\text{NH}}$  bands in the region 3217–3421  $\text{cm}^{-1}$ . Upon complexation,  $\nu_{\text{NH}}$  peaks disappear from the spectra of complexes **1–3** indicating the deprotonation of these groups in the ligand.<sup>[24]</sup> However for complexes **2** and **3** a new broad band appears in the region 3379–3381  $\text{cm}^{-1}$  indicating the formation of new  $\text{NH}_2$  group due to hydrolytic cleavage via  $\text{C}=\text{N}$  in the benzamidine ligands. In addition, the broad signal appearing at 3060  $\text{cm}^{-1}$  due to phenolic  $-\text{OH}$  group in ligand **H<sub>2</sub>L<sub>1</sub>** completely disappears during formation of complex **1**. Furthermore, a strong vibration observed at 1608–1620  $\text{cm}^{-1}$  for the ligands corresponding to  $\nu_{\text{C}=\text{N}}$  group is shifted to lower frequency in the spectrum of complex **1** and completely disappears in those of complexes **2** and **3** due to hydrolytic cleavage via  $\text{C}=\text{N}$  bond. A sharp band is observed in the range 820–843  $\text{cm}^{-1}$  ascribed to  $\nu_{\text{C}=\text{S}}$  group in the ligands, which is shifted to lower frequency upon complex **1** formation. However, the  $\nu_{\text{C}=\text{S}}$  stretching frequency of complexes **2** and **3** decreases by 20–30  $\text{cm}^{-1}$ , which suggests that the ligands are bound to the ruthenium(II)/copper(I) centre via the sulfur atom only. Parallel properties were witnessed for previously reported thiourea complexes.<sup>[25]</sup> These results clearly confirm that the coordination binding mode occurs through ONS donor (for **1**) and S donor (for **2** and **3**) atoms.

Proof of chelation can also be obtained from the NMR ( $^1\text{H}$ ,  $^{13}\text{C}$ ,  $^{31}\text{P}$ ) spectra of ligands and complexes. The data are summarized in Section 2 and the spectra depicted in Figures S1–S4. In the  $^1\text{H}$  NMR spectra, the signal due to the phenolic  $\text{C}_{\text{ar}}-\text{OH}$  and  $\text{C}_{\text{ar}}-\text{NH}$  groups of free ligand **H<sub>2</sub>L<sub>1</sub>** appear at 9.95 and 9.42 ppm, respectively. These groups are absent in the spectrum of **1**, supporting the deprotonation and coordination via oxygen and nitrogen atom to the ruthenium(II) ion.<sup>[2]</sup> This fact confirms the double

deprotonation of the ligand which is also confirmed by the IR data. In the free ligand **HL<sub>2</sub>**, the signal due to  $\text{C}_{\text{ar}}-\text{NH}$  group appears as a broad singlet at 6.93 ppm. But for **2** and **3**,  $\text{C}_{\text{ar}}-\text{NH}$  group signal completely disappears and new  $-\text{NH}_2$  peak appears in the range 8.17–8.21 ppm due to hydrolytic cleavage via  $\text{C}=\text{N}$  bond. Moreover, the proton signals of the two methylene groups for ligands and complexes, which should consequently be two quartets, appear as four well-separated multiplet resonances at 3.52–3.94 ppm. This pattern of the methylene signals has previously been rationalized by the rigid structure of the tertiary amine group, which makes the methylene protons magnetically non-equivalent with respect to their axial and equatorial positions.<sup>[9]</sup> Furthermore two triplet signals at 1.15–1.62 ppm for the methyl groups in  $\text{N}(\text{CH}_2\text{CH}_3)_2$  are observed in the spectra of ligands and complexes. In addition, the spectra of ligands and complexes show a series of overlapping multiplets for aromatic protons at 6.43–7.89 ppm.

The  $^{13}\text{C}$  NMR spectra show the expected signals in the appropriate regions. For the uncoordinated ligands, the  $\text{C}=\text{N}$  and  $\text{C}=\text{S}$  signals of **H<sub>2</sub>L<sub>1</sub>** and **HL<sub>2</sub>** appear in the regions around 149.36–155.41 and 187.08–189.61 ppm, respectively. Upon the coordination and formation of new ruthenium(II)/copper(I) complexes, a downfield shift is observed for the signals of  $\text{C}=\text{N}$  (around 6–10 ppm), while  $\text{C}=\text{S}$  carbon signals appear in the upfield region between 169.19 and 177.69 ppm.<sup>[26,27]</sup> These are consistent with ONS (for **1**) or S (for **2** and **3**) coordination and deprotonation as well as  $\text{C}=\text{N}$  cleavage of benzamidine ligands. The  $\text{C} \equiv \text{O}$  carbon resonating region at 203.01–204.12 ppm is comparable with that of reported ruthenium carbonyl complexes.<sup>[28]</sup> In addition, a couple of signals appear at 13.21–49.61 ppm for the  $\text{CH}_2$  and  $\text{CH}_3$  carbons. Furthermore, the aromatic carbons appear in the region 117.62–132.83 ppm for all the complexes.

The coordination of the triphenylphosphine as co-ligands and their configuration in the new complexes **1–3** are confirmed from analysis of  $^{31}\text{P}$  NMR spectra (Figures S5–S7). The appearance of only one sharp singlet at 36.98 and 34.83 ppm for ruthenium(II) complexes **1** and **2** suggests the presence of two magnetically equivalent triphenylphosphines *trans* to each other.<sup>[29]</sup> The appearance of one sharp singlet observed at  $-3.80$  ppm for complex **3** suggests the presence of two magnetically equivalent triphenylphosphines *cis* to each other.<sup>[30]</sup>

The UV–visible spectra of the complexes (Figure S8) were recorded in DMSO solution for different time intervals (0–12 h). The obtained spectra are similar, suggesting that complexes **1–3** retain their structure in solution within the timeframe used for the biological experiments. Electronic spectra of the complexes display intense absorptions in the visible and UV regions. The absorptions in the UV region are assignable to transitions within the ligand orbitals. The bands around 238–273 nm are assigned to ligand-centred

$\pi \rightarrow \pi^*$  and  $n \rightarrow \pi^*$  transitions. The absorption maxima located in the range 307–333 nm are assigned to  $S(\pi\pi) \rightarrow M(d\pi)$  ( $M = Ru^{2+}$ ) ligand-to-metal charge transfer (LMCT) transition for **1** and **2** and  $M(d\pi) \rightarrow S(\pi\pi)$  ( $M = Cu^+$ ) metal-to-ligand charge transfer (MLCT) transition for **3**.<sup>[31]</sup> Furthermore, the complexes show broad bands at 420–474 nm, attributed to the d–d transition bands of spin-paired  $d^{6f}$  (complexes **1** and **2**) species with a distorted octahedral structure. The geometry of the complexes was further confirmed using single-crystal X-ray diffraction analyses.

Information about the composition and stability of the complexes was also acquired from ESI-MS (in positive-ion mode) spectral studies. The ESI-MS data for complexes **1–3** are listed in Section 2 and spectra depicted in Figures S9–S11. Out of these, **1–3** display their molecular-ion peaks at  $m/z$  980.4, 822.3 and 721.3, respectively, assigned to  $[M]^+$  for **1** and  $[M - Cl]^+$  for **2** and **3** which reveal that the identity of the complexes is retained in solution. The observed isotopic distributions and their simulation patterns are in good agreement with the assigned formulations.

### 3.3 | Single-Crystal X-ray diffraction studies

Single-crystal X-ray diffraction studies of  $H_2L_1$  and **1–3** confirm the conclusions drawn from the spectroscopic studies. To gain insight into the coordination chemistry and structural parameters of these compounds, good-quality single crystals were isolated by slow evaporation of a concentrated methanol–chloroform solution and characterized by X-ray diffraction. Details of the data collection, solution and refinement are gathered in Section 2 and Table 1. ORTEP views of  $H_2L_1$  and the complexes (30% probability ellipsoids) along with a partial atom numbering scheme are shown in Figures 1–4 and important bond lengths and angles for the complexes are summarized in Table 2.

Figure 1 depicts the molecular structure of  $H_2L_1$ . It crystallizes in the triclinic  $P\bar{1}$  space group.  $H_2L_1$  shows

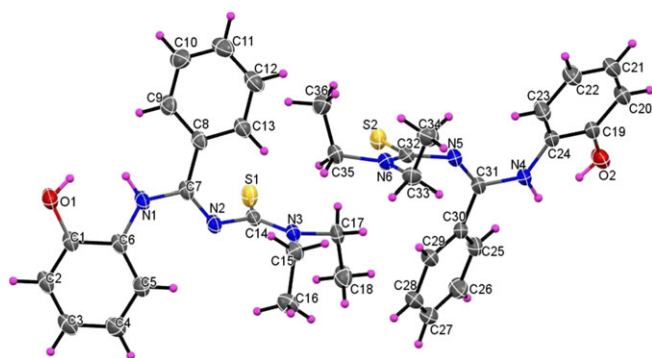


**FIGURE 1** Perspective view (30% probability ellipsoids) of  $H_2L_1$  with atom numbering scheme. Compound  $H_2L_1$  showing two independent molecules

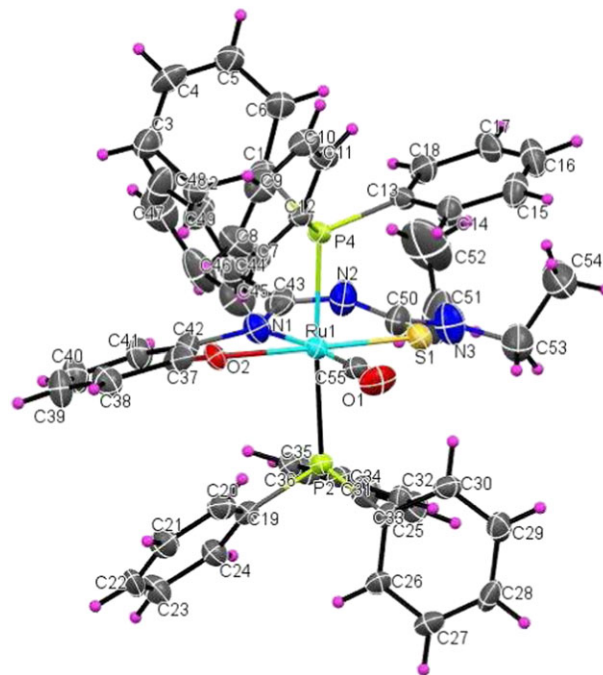


**FIGURE 2** Perspective view (30% probability ellipsoids) of complex **1** with atom numbering scheme

two independent molecules within the unit cell. The C–N and C=N bond distances (Table 2) found in  $H_2L$  agree well with that reported for other similar ligands containing C–N/C=N bonds. The thione form is confirmed by the bond length of C(14)–S(1) (1.696 Å) and C(32)–S(2) (1.693 Å) which are very close to a formal C=S bond length (1.60 Å). While C(7)–N(1) bond (1.289 Å) has only partial double bond character. This is found in all similar ligands and suggests that the proton is mainly located at the N1 atom. The configuration of  $H_2L_1$  is described as *E*, *dZ* configuration, which has also been found in some related ligands.<sup>[2,32]</sup> The *E*, *dZ* configuration is obtained due to intramolecular hydrogen bond between O1 and S1 atoms. In addition,  $H_2L_1$  contains one intramolecular hydrogen bond which creates a pseudo-hydroxo bridged binuclear structure (Figure S12).

Perspective views of complexes **1–3** with atomic numbering scheme are depicted in Figures 2–4, while selected bond lengths and angles are given in Table 2. Complexes **1–3** crystallize in the orthorhombic, monoclinic and triclinic  $P2_12_12_1$ ,  $P2_1/c$  and  $P\bar{1}$  space groups, respectively. In **1**, the coordination geometry around the ruthenium ion is hexacoordination with an octahedral geometry, where the basal plane is constructed with nitrogen, phenolic oxygen and thiolate sulfur atoms of the ligand in a bidentate tridentate fashion. The remaining apical coordination sites are filled by a carbonyl group and two triphenylphosphines *trans* to each other. The ONS chelated benzamidine ligand coordinates in a dibasic tridentate manner to the ruthenium(II) ion forming a stable six-/five-membered chelate ring. The ruthenium(II) ion is therefore sitting in a core  $RuCONSP_2$

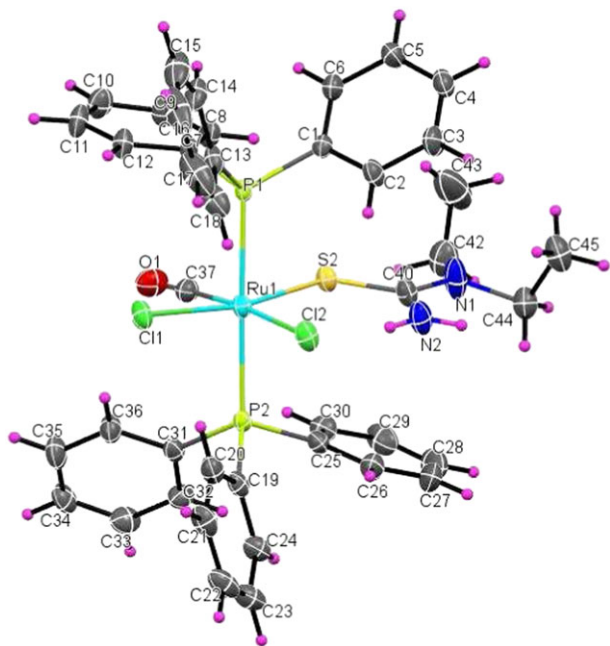


FIGURE 3 Perspective view (30% probability ellipsoids) of complex **2** with atom numbering scheme

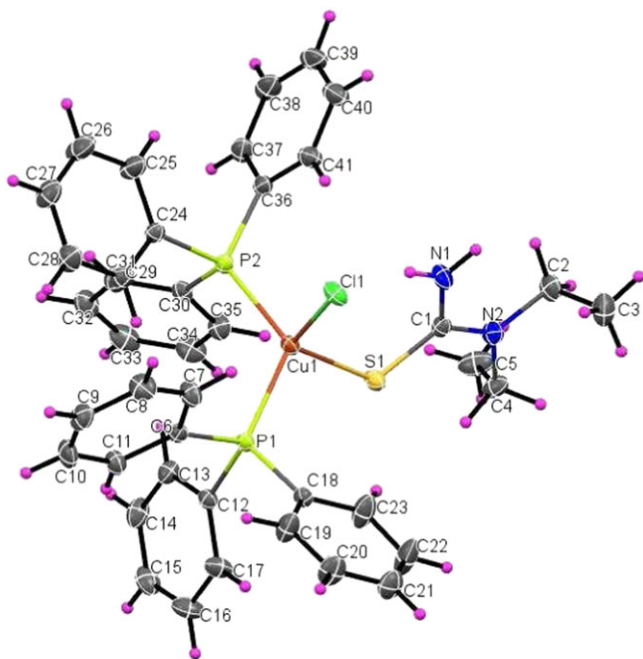


FIGURE 4 Perspective view (30% probability ellipsoids) of complex **3** with atom numbering scheme

coordination environment, which is distorted octahedral in nature as reflected in all the bond parameters around ruthenium. In **1**, the *trans* angles are [P(2)–Ru(1)–P(4)] 175.92(8)° and [O(2)–Ru(1)–S(1)] 171.93(16)°. The carbonyl group is *trans* to the coordinated N(1) atom [N(1)–Ru(1)–C(55)] with an angle of 171.7(3)°. Though the PPh<sub>3</sub> ligands usually prefer to occupy mutually *cis* position for better  $\pi$ -

interaction, in this complex the presence of CO, a stronger  $\pi$ -acidic ligand might have forced the bulky PPh<sub>3</sub> ligands to take *trans* position for steric reasons. The *trans* angles deviate from linearity and N(1), S(1) (six-membered ring) leads to small N(1)–Ru(1)–S(1) bite angle of 94.50(19)°. The ruthenium–ligand distances, namely C(55)–Ru(1) 1.863(10) Å, O(2)–Ru(1) 2.161(5) Å, N(1)–Ru(1) 2.166(7) Å, S(1)–Ru(1) 2.345(2) Å, P(2)–Ru(1) 2.402(19) Å, P(4)–Ru(1) 2.403(2) Å, found in **1** agree well with those reported for other similar ruthenium(II) complexes containing triphenylphosphine in *trans* position and the carbonyl group (CO) is *trans* to the nitrogen atom. The same phenomenon occurred with rhenium complexes in different oxidation states containing the same type of benzamidines.<sup>[33]</sup>

In complex **2**, the facile cleavage of the C=N bond during reaction of HL<sub>2</sub> with ruthenium(II) precursor is unexpected and seems to be metal-induced hydrolytic cleavage as shown in Scheme 2. The coordination geometry around ruthenium (II) ion exhibits hexa-coordination with an octahedral geometry, where the basal plane is constructed with only thiolate sulfur atom of the unexpected cleaved HL<sub>2</sub> in a neutral monodentate fashion. In complex **2**, the remaining apical coordination sites are filled by a carbonyl group, chlorine atom and two triphenylphosphines *trans* to each other. The ruthenium atom is in a distorted octahedral environment with *trans* angles of [P(2)–Ru(1)–P(1)] 178.18(6)° and [Cl(1)–Ru(1)–S(2)] 167.54(6)°. The carbonyl group is *trans* to the coordinated Cl(2) atom [Cl(2)–Ru(1)–C(37)] with an angle of 173.9(2)°. The other two axial sites are occupied by a carbonyl group and one chlorine atom with Ru(1)–(37) and Ru(1)–Cl(2) distances of 1.827(7) and 2.4748(16) Å. The CO group occupies the site *trans* to the Cl (C(37)–Ru(1)–Cl(2), 173.8(2)°). This may be a consequence of strong Ru(II)  $\rightarrow$  CO back donation as indicated by the short Ru(1)–C(37) (1.827(7) Å) bond and low CO stretching frequency (1952 cm<sup>-1</sup>), which prefers  $\sigma$  or  $\pi$  weak donor groups occupying the site opposite to CO to favour the d– $\pi$  back donation. The ruthenium–ligand distances, namely Ru(1)–S(2) 2.4096(16) Å, Ru(1)–C(37) 1.826(7) Å, Ru(1)–P(1) 2.4025(16) Å, Ru(1)–Cl(1) 2.4432(16) Å, Ru(1)–Cl(2) 2.4750(16) Å, Ru(1)–P(2) 2.3964(17) Å, found in complex **2** agree well with those reported for other similar ruthenium (II) complexes containing triphenylphosphine in *trans* position and the carbonyl group (CO) is *trans* to the chlorine atom.<sup>[34]</sup> In addition, complex **2** contains one intramolecular hydrogen bond which creates a pseudo-chloro bridged binuclear structure (Figure S12). Therefore, based on the crystal structures and spectroscopic properties, we propose a conceivable mechanism for the formation of complex **2** as shown in Scheme 3.

In complex **3**, the coordination geometry around copper (I) ion exhibits four-coordination with tetrahedral geometry, where the basal plane is constructed with only thiolate sulfur atom of the unexpected cleaved H<sub>2</sub>L<sub>1</sub> and HL<sub>2</sub>. In complex

**3**, the remaining apical coordination sites are filled by chlorine atom and two triphenylphosphine *cis* to each other. The copper atom is in a tetrahedral environment with *cis* angles of P(1)–Cu(1)–P(2) 121.64(2)°, P(2)–Cu(1)–S(1) 110.80(2)° and P(2)–Cu(1)–Cl(1) 104.72(2)°. The copper–ligand distances, namely Cu(1)–Cl(1) 2.3911(6) Å, Cu(1)–S(1) 2.3684(6) Å, Cu(1)–P(1) 2.2986(5) Å, Cu(1)–P(2) 2.3094(6) Å, found in complex **3** agree well with those reported for other similar copper(I) complexes containing triphenylphosphine in *cis* position.<sup>[30,35]</sup> In addition, complex **3** contains one intramolecular hydrogen bond which creates a pseudo-chloro bridged binuclear structure (Figure S12). The unit cell packing diagram of the compounds is shown in Figure S13.

### 3.4 | Computational details for theoretical calculations

To obtain further insight into the electronic structures of the compounds, optimizations of **H<sub>2</sub>L<sub>1</sub>** and **1–3** have been carried out using the DFT/B3LYP methodology. The molecular geometries of **H<sub>2</sub>L<sub>1</sub>** and **1–3** in the gas phase singlet states have been optimized and the selected bond parameters are given in Table 2. Vibrational frequency calculations were performed for each of these compounds, to ensure that the optimized geometries represented the local minima of the potential energy surface and that only positive eigenvalues were found. In general, the optimized geometry for the compounds reproduces the overall details of the X-ray structure with a reasonable agreement. Contour plots of the HOMO and LUMO of the compounds and the energy gap are shown in Figure 5. The lowering of the HOMO–LUMO band gap is essentially a consequence of the large stabilization of the LUMO due to the strong electron-accepting ability of the electron-acceptor group. As one can see from Figures 5 and S14, and the data collected in Table S17, the electron density of HOMO in **1** is mainly localized on the **H<sub>2</sub>L<sub>1</sub>** ligand (67% **H<sub>2</sub>L<sub>1</sub>** + 11% d<sub>Ru</sub>). While in the case of **2** and **3**, the share of 1,1-DT ligand decreases with the increased involvement of the metal ion orbitals with the significant participation of chloride ligand in the case of **3**. Similar situation occurs in the case of the LUMO which in **1** is localized mainly on the **H<sub>2</sub>L<sub>1</sub>** ligand whereas in **2** in phosphine (52%) and d<sub>Ru</sub> (35%) orbitals and in the case of **3** the LUMO comprises the PPh<sub>3</sub> ligands. Thus, taking into account the composition of the HOMO and LUMO, it can be assumed that the lowest energy electronic absorption bands, with maxima above 400 nm, have MLCT character. However, in the case of **3** the participation of the inter-ligand charge transfer transitions ( $\pi_{\text{Cl}} \rightarrow \pi^*_{\text{PPh}_3}$ ) is significant, which confirms the high value of the absorption coefficient determined for the band with maximum at 474 nm ( $\epsilon = 10400$ ). On the other hand, for tetrahedral complex the share of ligand p orbitals in the HOMO is justified because of the symmetry, and hence

the intensity of electronic transitions is much greater than in the case of octahedral ones. Similarly, the high value of the absorption coefficient of the lowest energy absorption band in the case of **1** also confirms the ligand-to-ligand charge transfer character of this absorption band. The low intensity of the absorption band with maximum at 420 nm in the case of **2** results from the considerable participation of ruthenium d orbitals in HOMO and LUMO levels. So, the lowest energy absorption band has MLCT character with admixture of d → d (LF) transitions.

## 3.5 | DNA interaction studies

### 3.5.1 | Stability of compounds

To carry out a biological evaluation of complexes, checking their stability in solution is an important requirement.<sup>[36–38]</sup> To check the stability of complexes **1–3**, electronic spectra have been recorded in DMSO at four different time points (0–12 h) through the UV–visible absorption method. The UV–visible spectral results (Figure S4) do not reveal any appreciable changes in either the intensity or the position of the absorption bands in DMSO solution. This demonstrates that the complexes retain a stable structure under physiological-type conditions.

### 3.5.2 | Fluorescence emission titration

Fluorescence emission titration offers an effective method for following binding of metal complexes with CT-DNA.<sup>[39]</sup> Intercalation of metal complexes with base pairs of DNA is usually shadowed by a hypochromic shift with a small red/blue shift. On the other hand, non-intercalative, electrostatic interactions or damage of the DNA double helix result in a hyperchromic shift. From the fluorescence emission titration curves, the binding mode and propensity of **1–3** were studied in the absence and presence of CT-DNA at different increasing concentrations.

From the emissive titration spectra (Figure 6), it is apparent that upon the addition of increasing concentrations of CT-DNA (0–50 μM) to a solution of **1–3** there is hypochromism of about 13.24% (358 nm), 35.12% (355 nm) and 25.04% (288 nm), respectively, along with a small red shift (*ca* 2–3 nm). The observed hypochromism is due to an intercalative mode of binding involving a strong stacking interaction between extended aromaticity of the ligands and the base pairs of DNA. Based on the emission enhancement, the intrinsic binding constant was obtained according to the Scatchard equation:

$$C_b = \frac{C_t(F-F_0)}{F_{\text{max}}-F_0}$$

where  $C_t$  is the total compound concentration,  $F$  the observed fluorescence emission intensity at given DNA concentration,  $F_0$  the intensity in the absence of DNA and  $F_{\text{max}}$  the fluorescence of the totally bound compound. The fluorescence

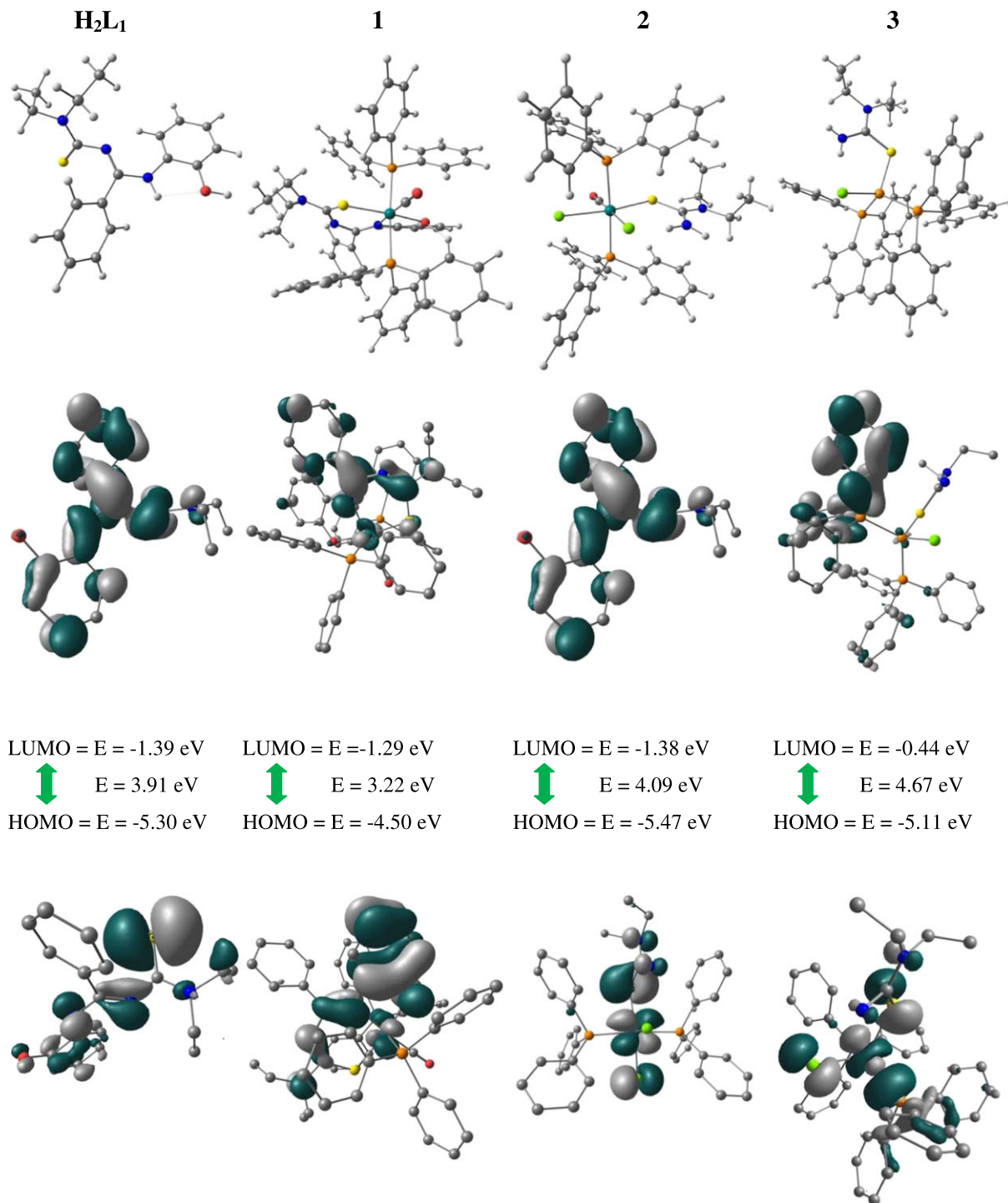


**FIGURE 5** Frontier molecular orbitals of the compounds and their HOMO–LUMO energy gap and ground state optimized geometry (top). For the HOMOs and LUMOs hydrogen atoms are omitted for clarity. Positive and negative regions are shown in grey and green, respectively

spectra of the tested compounds with increasing concentration of CT-DNA are depicted in Figure 6. Intrinsic binding constant ( $K_b$ ) was cast in the form of a Scatchard plot of  $r/C_f$  versus  $r$ , where  $r$  is the binding ratio of  $C_b/[DNA]$  and  $C_f$  is the free ligand concentration.  $K_b$  and binding site size ( $s$ ) values for **1–3** with CT-DNA are listed in Table 3. From available data it is concluded that the complexes bind to DNA via intercalative mode similar to earlier reports,<sup>[40]</sup> where the order of DNA binding affinity is **3** > **1** > **2**. This may be

ascribed to the presence of different functional groups in the complexes and the lower value of  $s$  indicates intercalative binding mode. Nevertheless, the binding mode needs to be confirmed through further experiments.

### 3.5.2.1 | EB displacement study

The fluorescence spectral technique is an effective method for studying the interaction of metal complexes with DNA.

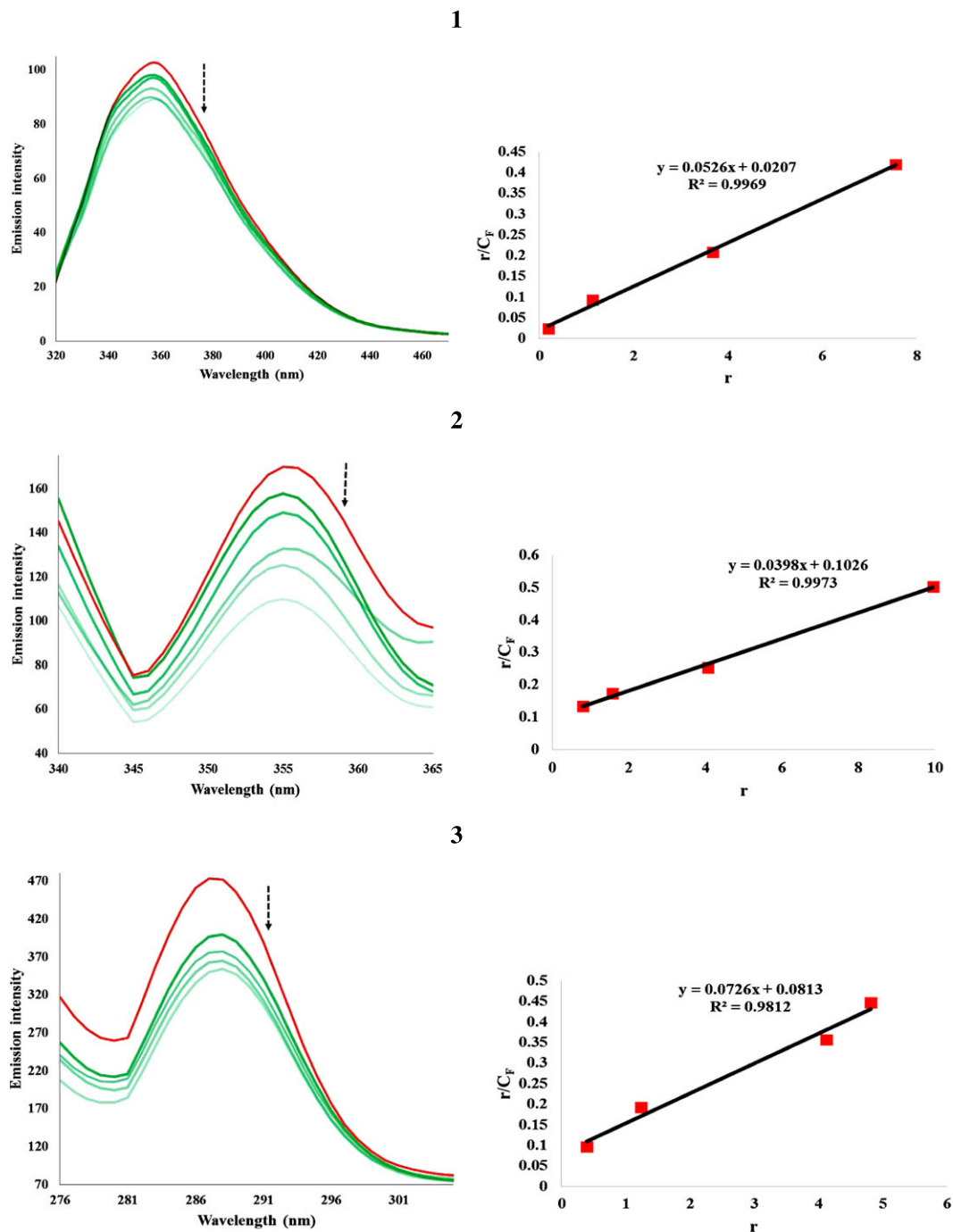


**FIGURE 6** Fluorescence titrations of complexes 1–3 (25  $\mu\text{M}$ ) with CT-DNA (0–50  $\mu\text{M}$ ) (left). Scatchard plots of  $r/C_F$  versus  $r$  for complexes 1–3 (right)

Hence fluorescence quenching experiments with EB-bound DNA were undertaken to understand the mode of DNA interaction with complexes 1–3. EB, a cationic conjugated

planar molecule, is a well-known DNA intercalator. It is known that EB emits intense fluorescence in the presence of DNA owing to its strong intercalation between adjacent base pairs. The extent of fluorescence quenching of EB by competitive displacement from DNA is a measure of the strength of the interaction between the second molecule and DNA.<sup>[41]</sup> The emission spectra of EB bound to CT-DNA in the absence and presence of complexes 1–3 are shown in Figure 7.

As the concentration of complexes increases, the emission band at 606 nm (Figure 7) for EB exhibits hypochromism of

**TABLE 3** Fluorescence spectral parameters for complexes 1–3 bound to CT-DNA

Complex	$K_b$	$s$	$K_{sv}$	$K_{app}$
1	$5.26 \times 10^4$	0.02	$2.36 \times 10^4$	$3.17 \times 10^5$
2	$3.98 \times 10^4$	0.10	$1.19 \times 10^4$	$6.30 \times 10^5$
3	$7.26 \times 10^4$	0.08	$1.03 \times 10^5$	$7.25 \times 10^6$

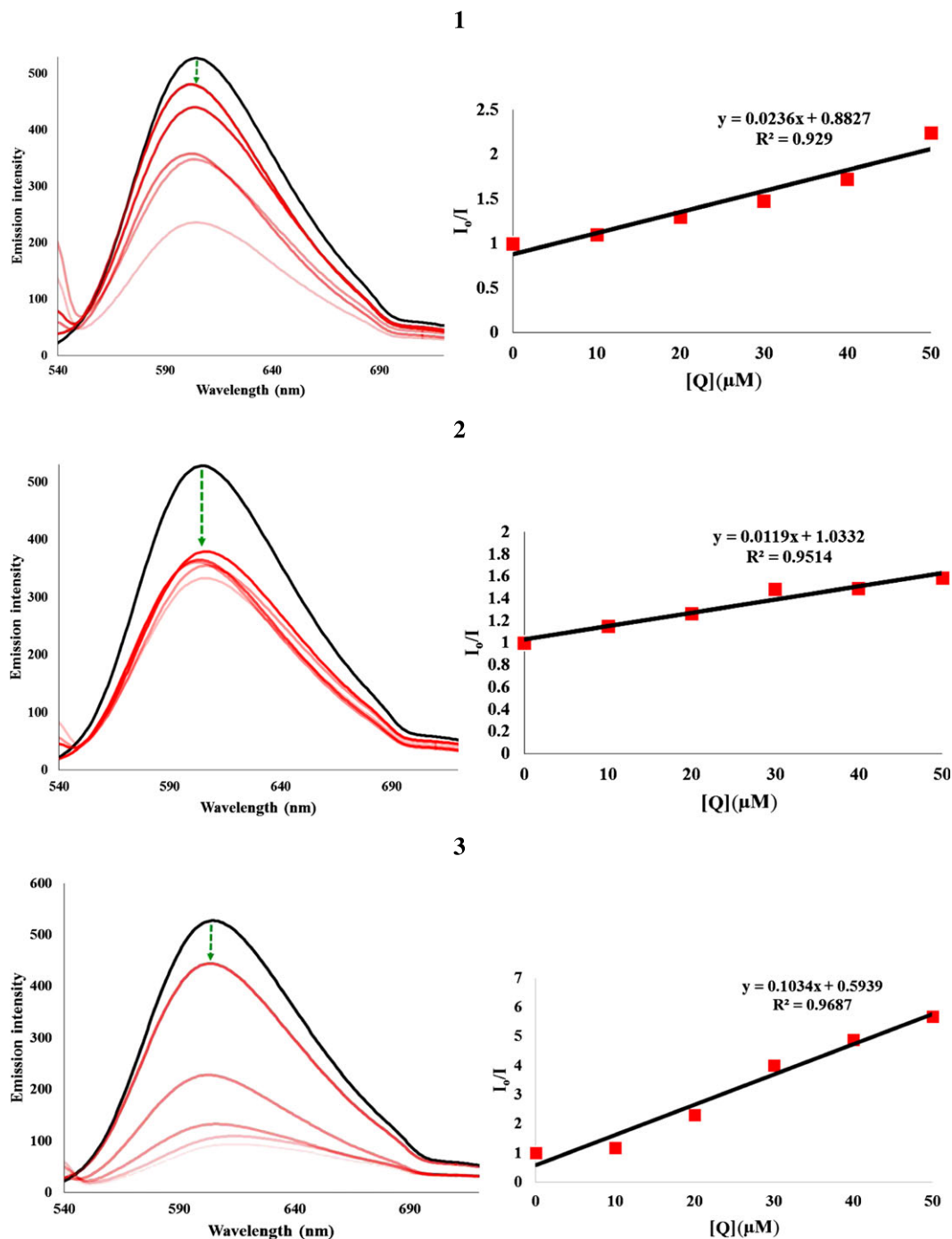


FIGURE 7 Fluorescence titrations of 1–3 (0–50  $\mu\text{M}$ ) with EB-bound CT-DNA (7.5  $\mu\text{M}$ ) (left). Scatchard plots of  $I_0/I$  versus  $[Q]$  for complexes 1–3 (right)

up to 53.39, 36.87 and 82.34% with a slight red/blue shift from the initial fluorescence intensity. Further, the quenching parameters for the magnitude of interaction were ascertained from the classical Stern–Volmer equation:

$$\frac{I_0}{I} = 1 + K_{sv}[Q]$$

where  $I_0$  and  $I$  are the emission intensities of EB-bound CT-DNA in the absence and presence of the quencher (complex) concentration  $[Q]$ , respectively, which gives the Stern–Volmer quenching constant ( $K_{sv}$ ). The quenching constant values (Table 3) were obtained from the slope of

a plot of  $I_0/I$  versus  $[Q]$  as shown in Figure 7. From these results it is evident that EB is displaced quite efficiently from the binding sites of CT-DNA by the complexes that also strongly bind with DNA.

Further, apparent DNA binding constants ( $K_{app}$ ) have been calculated using the following equation:

$$K_{EB}[EB] = K_{app}[M_{50\%}]$$

where  $K_{EB} = 1.0 \times 10^{-7} \text{ M}^{-1}$  is the DNA binding constant of EB,  $[EB]$  is the concentration of EB (7.5  $\mu\text{M}$ ) and  $[M_{50\%}]$  is the concentration of the compound used

to obtain a 50% reduction in fluorescence intensity of DNA pretreated with EB. The  $K_{app}$  values for **1–3** are given in Table 3. The DNA binding ability of the compounds follows the order **3** > **1** > **2**, which is in accord with the results obtained from the fluorescence spectral studies discussed above, and we conclude that all the complexes may bind with DNA via intercalation.

### 3.5.3 | Viscometric study

These measurements were implemented to authenticate and further clarify and investigate the conformational changes of DNA upon interaction with the metal complexes. These measurements can lend strong support in favour of intercalative binding. In general, this method popularly accepts that a partial and/or non-classical intercalation of a ligand could bend (or kink) the DNA helix, reducing its effective length concomitantly.<sup>[42]</sup> The viscosity of CT-DNA increases when a compound binds with DNA in intercalating mode but remains unchanged when a compound binds with DNA in electrostatic mode. From these considerations, this measurement could lend strong support in favour of intercalative binding. The changes in the relative specific viscosity of CT-DNA (200  $\mu\text{M}$ ) in the presence and absence of complexes **1–3** (0–120  $\mu\text{M}$ ) were plotted as  $(\eta/\eta_0)^{1/3}$  versus [compound]/[DNA]. The relative viscosity of DNA solution increases upon addition of all complexes in the order **3** > **1** > **2** (Figure 8). The viscosity changes might be considered evidence of all three complexes intercalate between the base pairs of CT-DNA. This result is consistent with our foregoing fluorescence spectral studies.

## 3.6 | BSA interaction studies

### 3.6.1 | UV-visible spectral study

Serum albumins are the most extensively studied and applied proteins due to their ability to transport amino acids and drug molecules. Interaction of metallodrugs with proteins is significant for obtaining information about their properties such as uptake, bio-distribution, overall toxicity, mechanism of action and shuttling of complexes to cancer cells. Therefore, studies

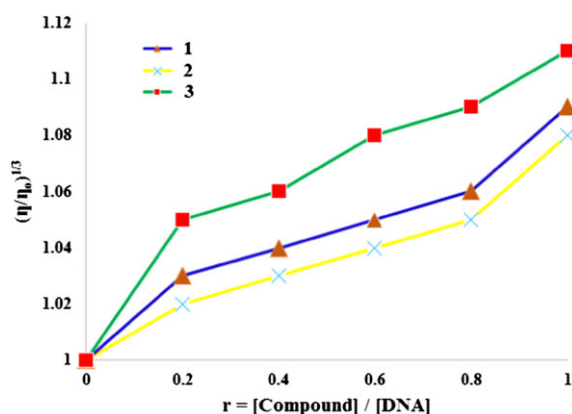


FIGURE 8 Relative viscosity  $(\eta/\eta_0)^{1/3}$  of CT-DNA in Tris-HCl buffer solution in the presence of complexes **1–3** in increasing amounts ( $r = 0–1$ )

of the binding of a drug with a protein will facilitate interpretation of the metabolism and transporting processes of the drug and explain the affiliation between structures and functions of a protein.<sup>[43]</sup> In this regard, BSA is utilized extensively because of its structural homology with human serum albumin. The type of interaction between complexes **1–3** and BSA, whether static or dynamic quenching, was determined from UV-visible absorption studies. The absorption spectra of BSA solutions (1  $\mu\text{M}$ ) in the absence and presence of **1–3** (25  $\mu\text{M}$ ) are shown in Figure 9. The addition of the complexes causes an increase in the intensity of BSA absorption at *ca* 280 nm with a small blue shift of about 2 nm, suggesting a static interaction between complexes and BSA. These UV-visible results clearly indicate a static interaction from the formation of a complex between the quencher (**1–3**) and the fluorophore (BSA) in the ground state.

### 3.6.2 | Fluorescence spectral study

In the fluorescence study, a solution of BSA (1  $\mu\text{M}$ ) was titrated with increasing concentrations of **1–3** (0–50  $\mu\text{M}$ ) in the range 290–440 nm ( $\lambda_{ex} = 280$  nm) with negligible redshift. The observed red shift is mainly due to the active site in protein hydrophobic environment. Figure 10 demonstrates the effect of increasing concentration of complexes on the fluorescence emission of BSA. The fluorescence quenching constant ( $K_q$ ) is defined by the following Stern-Volmer equation:

$$\frac{I_0}{I} = 1 + K_{sv}[Q] = 1 + K_q\tau_0[Q]$$

where  $I_0$  and  $I$  are the fluorescence intensity in the absence and presence of the quencher, respectively.  $K_q$  is the quenching rate constant,  $\tau_0$  is the fluorescence lifetime of biopolymer BSA ( $\tau_0 = 10^{-8}$  s)<sup>[43]</sup> and  $K_{sv}$  and  $[Q]$  are the Stern-Volmer quenching constant and the concentration of quencher, respectively.  $K_q$  values were calculated from plots of  $I_0/I$  versus  $[Q]$  (Figure 10). It can be seen that the  $K_q$  value of BSA is higher than  $1.0 \times 10^{12}$ , which is much higher than

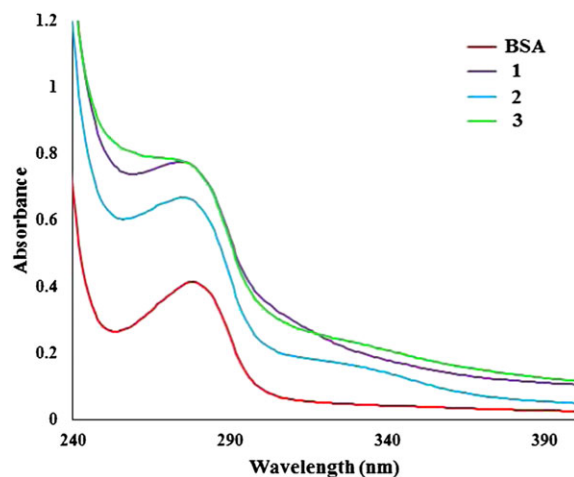
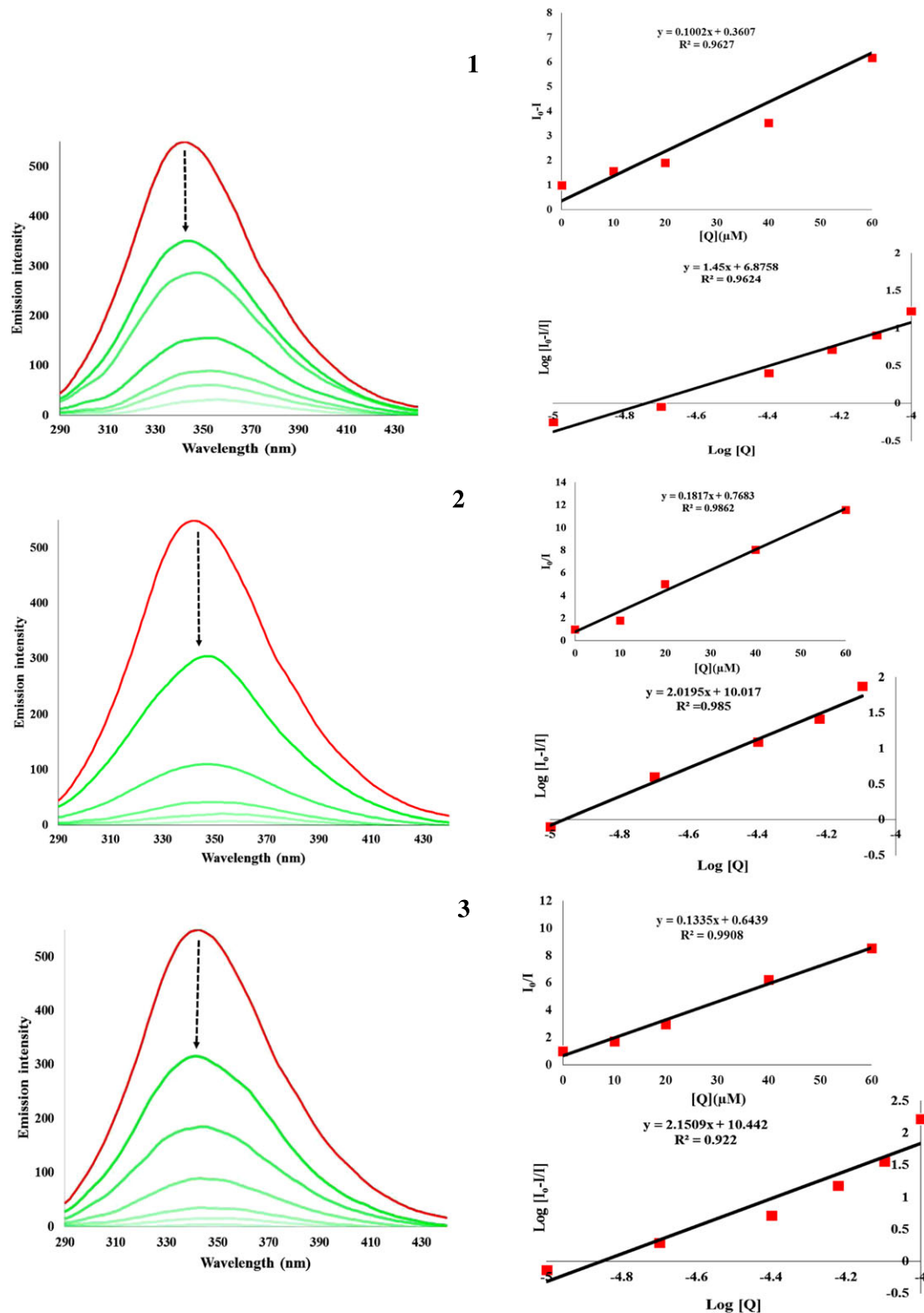


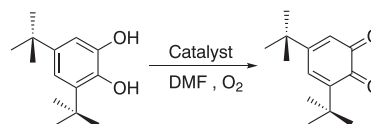
FIGURE 9 Absorption spectra of complexes **1–3** with BSA



**FIGURE 10** Fluorescence titrations of complexes 1–3 (0–50  $\mu\text{M}$ ) with BSA (1  $\mu\text{M}$ ) (left). Stern–Volmer plots of  $I_0/I$  versus  $[Q]$  and Scatchard plots of  $\log[(I_0 - I)/I]$  versus  $\log[Q]$  for complexes 1–3 (right)

**TABLE 4** Quenching parameters of BSA for complexes 1–3

Complex	$K_{sv}$	$K_q$	$K_{bin}$	n
1	$1.002 \times 10^5$	$1.002 \times 10^{13}$	$7.50 \times 10^6$	1.45
2	$1.187 \times 10^5$	$1.187 \times 10^{13}$	$1.03 \times 10^{10}$	2.01
3	$1.335 \times 10^5$	$1.335 \times 10^{13}$	$2.77 \times 10^{10}$	2.10



**SCHEME 5** Catalytic oxidation of 3,5-DTBC to 3,5-DTBQ in DMF in oxygen atmosphere

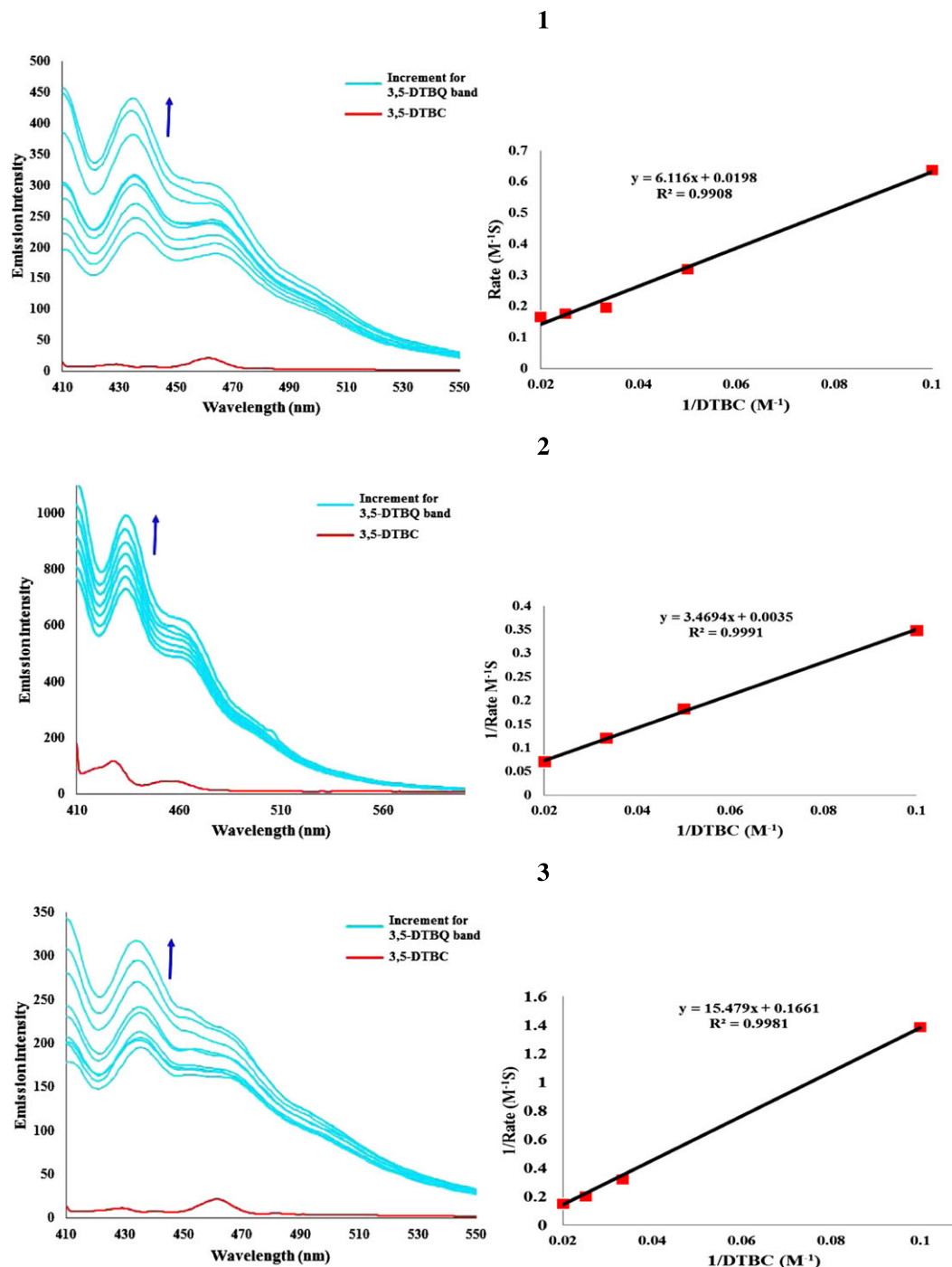


FIGURE 11 Oxidation of 3,5-DTBC by complexes 1–3 monitored by fluorescence spectroscopy (left). Lineweaver–Burk plots for tested compounds (right)

the molecular fluorescence diffusing constant as evident from Table 4. From the values of  $K_q$ , it is concluded that complex 3 interacts with BSA more strongly than the other complexes.

### 3.6.3 | Binding constant and binding site number.

The binding constant  $K_{bin}$  was calculated using the Scatchard equation:

$$\log\left(\frac{I_0 - I}{I}\right) = \log K_{bin} + n \log[Q]$$

where  $K_{bin}$  is the binding constant of the compound with BSA and  $n$  is the number of binding sites.  $K_{bin}$  and  $n$  have been found from plots of  $\log[(I_0 - I)/I]$  versus  $\log[Q]$  (Figure 10). The calculated  $K_{bin}$  and  $n$  are gathered in Table 4. The calculated value of  $n$  is around 2 indicating the existence of two binding sites available in BSA for all the complexes. The higher values of  $K_q$  and  $K_{bin}$  indicate strong interaction between the BSA protein and the complexes. It is noticed that the values of binding constant of the complexes follows the order  $3 > 2 > 1$ , suggesting that the complexes effectively bind with BSA and hence can have potential anticancer properties.

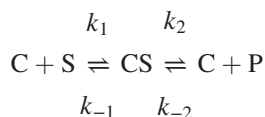
### 3.7 | Catechol oxidase study

In order to check the ability of complexes **1–3** to show catecholase mimic properties, the catalytic oxidation of 3,5-DTBC, which is taken as an exemplary substrate, showing a low quinone–catechol reduction potential, was carried out. In general, it is easy to oxidize and the bulky *tert*-butyl groups prevent further over-oxidation such as ring opening (Scheme 5). So far, only a limited number of ruthenium(II)/copper(I) complexes have been reported to mediate catalytic oxidation of 3,5-DTBC.<sup>[44]</sup>

The reactions were carried out at 30 °C in presence of air and monitoring was done by fluorescence spectroscopy. Complexes **1–3** ( $1 \times 10^{-4}$  M) were added to 100 equivalents of a DMF solution of 3,5-DTBC ( $1 \times 10^{-2}$  M) under aerobic conditions and the progress of the reaction was studied every 15 min up to 2 h. It is seen that on addition of 3,5-DTBC, a new band (Figure 11) appears and its intensity gradually increasing at 434 nm may be attributed to LMCT band due to the formation of the oxidized product 3,5-di-*tert*-butylbenzoquinone (3,5-DTBQ). Thus, the experiment clearly proves that the oxidation of 3,5-DTBC to 3,5-DTBQ is catalysed by the new complexes, as it is well established that 3,5-DTBQ shows a maximum at  $\lambda_{\text{emis}} = 434$  nm in pure DMF.

### 3.8 | Kinetic study of catecholase activity

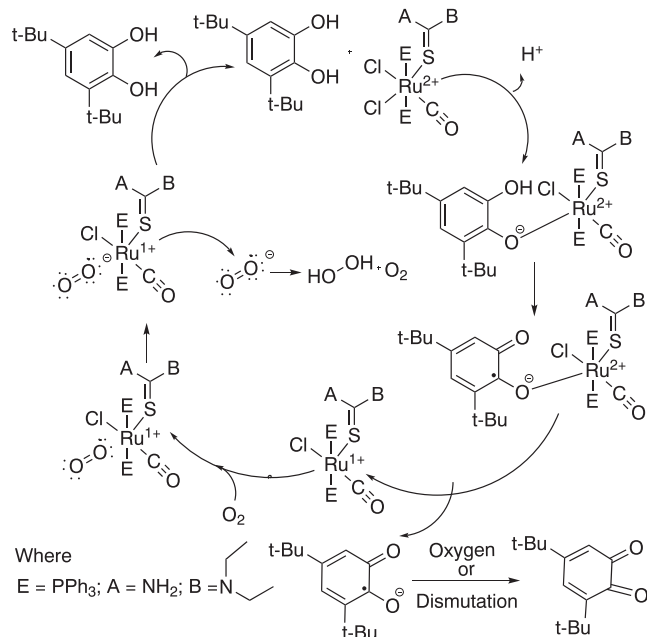
The rate constant of the catalyst was determined by the initial rate method. Furthermore, the catalytic behaviour showed saturation kinetics, and a treatment based on the Michaelis–Menten model seemed to be appropriate under excess substrate conditions. Plots of  $k_i$  versus [3,5-DTBC] give nonlinear curves of decreasing slope (Figure S15) which are best designated by the following equations:



$$V = \frac{V_{\text{max}}[S]}{K_M + [S]}$$

$$\frac{1}{V} = \frac{K_M}{V_{\text{max}}} \frac{1}{[S]} + \frac{1}{V_{\text{max}}}$$

A feasible mechanism of 3,5-DTBC oxidation promoted by catalysts **1–3** is shown in Scheme 6 based on the report of Chyn and Urbach.<sup>[45]</sup> Unfortunately we were unable to characterize the intermediates. However, when a mixture of starch–potassium iodide solution was added to a mixture of complexes and 3,5-DTBC, blue coloration formed, indicating that  $\text{H}_2\text{O}_2$  was produced during the course of reaction. It is



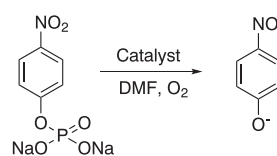
**SCHEME 6** Conceivable mechanism for the catalytic cycle of the oxidation of 3,5-DTBC

interesting to note that no blue coloration was observed in the absence of 3,5-DTBC.

According to the catecholase reaction mechanism (Scheme 6), an electron transfer occurs in the rate-determining step resulting in a substrate–catalyst 1:1 intermediate indicating that in the catalytic cycle there is only one ruthenium/copper ion accepting one electron from the substrate.<sup>[45]</sup> The Michaelis–Menten constant ( $K_m$ ) and maximum initial rate ( $V_{\text{max}}$ ) were determined by linearization using Lineweaver–Burk plots (Figure 11). The rate constants for dissociation of substrates S (i.e. turnover number,  $k_{\text{cat}}$ ) were calculated from graphs of  $1/V$  versus  $1/[S]$  (Figure 11), known as Lineweaver–Burk plots, using the above equation and all these parameters are listed in Table 5. Upon comparison of the data in Table 5, it might be stated that complex **2** is a highly efficient catalyst and has an appreciable turnover rate, and the order of their activity is  $2 > 1 > 3$ .

**TABLE 5** Kinetic parameters for the catecholase activity of complexes **1–3**

Catalyst	$K_m$ (M)	$V_{\text{max}}$ (M m <sup>-1</sup> )	$K_{\text{cat}}$ (h <sup>-1</sup> )
<b>1</b>	$3.08 \times 10^{-2}$	$5.05 \times 10^{-3}$	308
<b>2</b>	$9.88 \times 10^{-1}$	$2.85 \times 10^{-2}$	988
<b>3</b>	$9.31 \times 10^{-3}$	$6.02 \times 10^{-4}$	93



**SCHEME 7** Hydrolysis of 4-NPP to 4-NP ion in DMF in oxygen atmosphere

### 3.9 | Phosphate hydrolysis activity

Phosphates are widely found in biological organisms. Phosphate diesters such as DNA and RNA have metabolic intermediates that exist as phosphomonoesters.<sup>[46]</sup> Their kinetic stability makes monoesters particularly suitable for their biological roles. 4-NPP ester is negatively charged and under neutral conditions is very resistant towards hydrolysis. Therefore the development of artificial catalysts capable of cleaving phosphate ester bonds is of fundamental importance as they may find applications in gene technology or as therapeutic antisense oligonucleotides. Its hydrolytic tendency was investigated using emissive intensities by monitoring the time

evolution of *p*-nitrophenolate (4-NP) ion in DMF at  $\lambda_{\text{emis}} = 486 \text{ nm}$  ( $\lambda_{\text{ex}} = 435 \text{ nm}$ ) through a wavelength scan from 400 to 800 nm over 15 min intervals up to 2 h with 40 equivalents of substrate being used relative to the catalyst (Scheme 7).

### 3.10 | Kinetic study of phosphatase activity

In order to obtain the rate constant of the catalyst the initial rate method was used. Moreover, the catalytic behaviour showed saturation kinetics, and a treatment based on the Michaelis–Menten model seemed to be appropriate

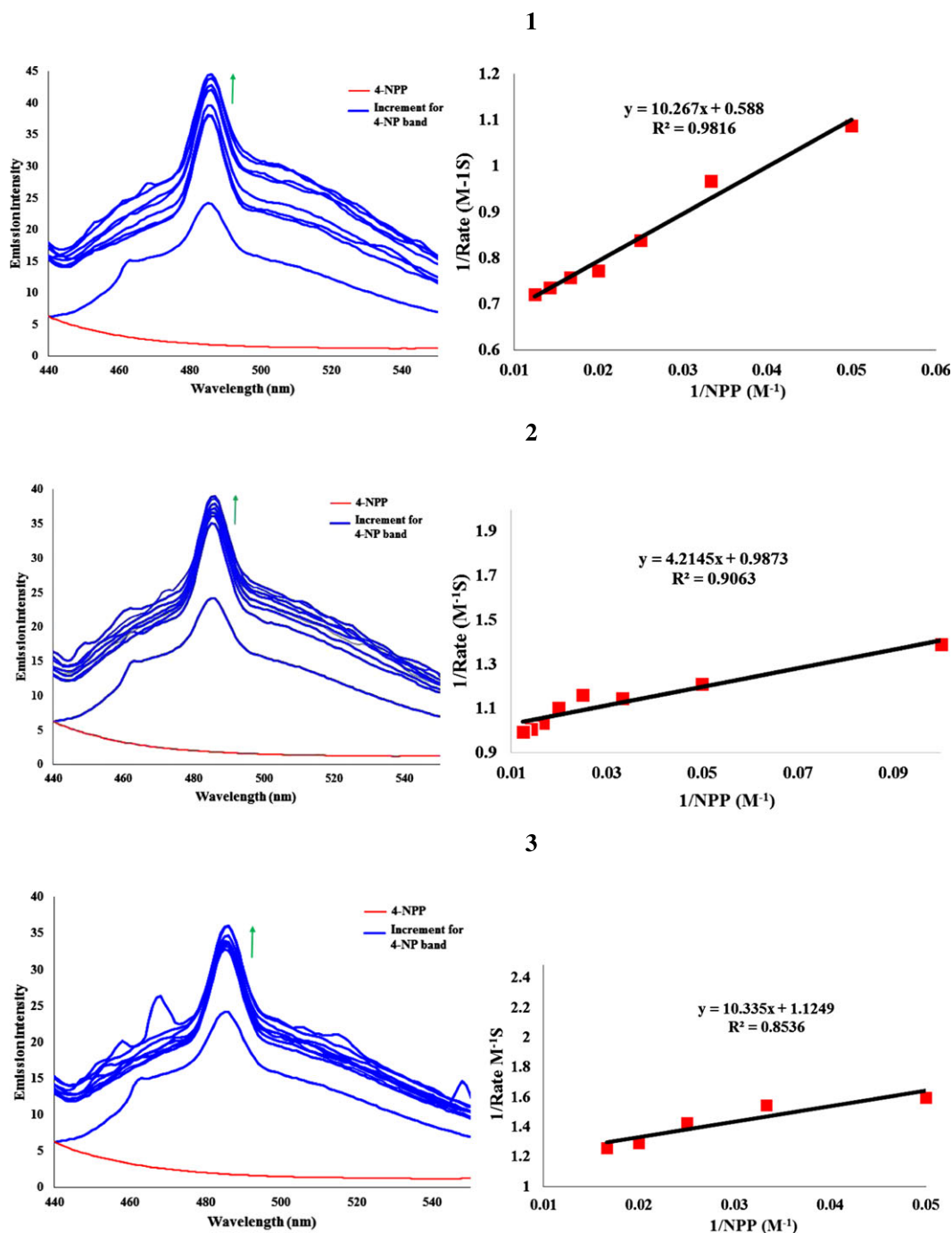


FIGURE 12 Hydrolysis of 4-NPP by complexes 1–3 monitored by fluorescence spectroscopy (left). Lineweaver–Burk plots for complexes 1–3 (right)

under excess substrate conditions. The dependence of the initial rate on the concentration of the substrate was monitored at the respective wavelength by fluorescence spectroscopy, which corresponds to the increase in 4-NP concentration (Figure 12). Plots of  $k_i$  versus [4-NPP] give nonlinear curves of decreasing slope (Figure S16) which are best designated by first-order kinetic equations. The rate versus concentration of substrate data were scrutinized on the basis of the Michaelis–Menten approach of enzymatic kinetics to get Lineweaver–Burk (double reciprocal) plots as well as the values of the various kinetic parameters  $V_{max}$ ,  $K_m$  and  $K_{cat}$ . The rate constant for dissociation of substrates S (i.e. turnover number,  $k_{cat}$ ) were calculated from the graphs of  $1/V$  versus  $1/[S]$  (Figure 12) using the kinetics equation and all these parameters are listed in Table 6. While comparing all these data it can be concluded that complex **3** is quite an efficient catalyst and has an appreciable turnover rate and the order of the activity is  $3 > 2 > 1$ . Therefore, based on the crystal structures, and physicochemical properties, it is concluded that the hydrolysis of 4-NPP follows the mechanism of catacholase activity.

### 3.11 | Anticancer activity *In Vitro*

#### 3.11.1 | Cancer cell growth inhibition (MTT assay)

The cytotoxicity of complexes **1–3** was determined using the MTT assay against normal Vero and cancer cell lines, namely human cervical cancer (HeLa), human hepatocellular carcinoma (HepG2) and human breast cancer (MCF-7) cell lines. Cells were exposed to a broad range of drug concentrations ( $10–100 \mu\text{g ml}^{-1}$ ) for 24 h, and the cell viability was quantified using the colorimetric method. The amount of cell proliferation significantly decreases in a dose-dependent manner on supplementation with complexes **1–3**, as observed within 24 h of incubation with respective cell lines (Figure 13). For comparison purposes, the cytotoxicity of cisplatin was evaluated under the same experimental conditions.<sup>[47,48]</sup> The results were analysed by means of cell inhibition expressed as  $IC_{50}$  values and are summarized in Table 7. As evident from Table 7, the  $IC_{50}$  values show that complex **3** exhibits slightly higher inhibitory effect than the other complexes towards the tested cancer cell lines. Moreover, the complexes display slightly less cytotoxic activity than cisplatin. Importantly, complexes **1–3** are less toxic towards the normal Vero cell line as is evident from the higher  $IC_{50}$  values (Table 7). On the basis of the  $IC_{50}$  values, the cytotoxicity of these complexes can be arranged in the order  $3 > 2 > 1$ . The cytotoxic

TABLE 6 Kinetic parameters for the phosphatase activity of complexes **1–3**

Catalyst	$K_m$ (M)	$V_{max}$ ( $M m^{-1}$ )	$K_{cat}$ ( $h^{-1}$ )
<b>1</b>	$1.74 \times 10^{-2}$	$1.70 \times 10^{-2}$	34.92
<b>2</b>	$4.26 \times 10^{-3}$	$1.01 \times 10^{-3}$	85.30
<b>3</b>	$9.18 \times 10^{-3}$	$0.88 \times 10^{-3}$	183.70

TABLE 7 *In vitro* cytotoxicity of compounds against normal and cancer cell lines

Compound	$IC_{50}$ ( $\mu\text{g ml}^{-1}$ ) <sup>a</sup>			
	Vero	HeLa	HepG2	MCF-7
<b>1</b>	$54.31 \pm 1.06$	$33.56 \pm 0.69$	$34.14 \pm 1.10$	$34.13 \pm 1.45$
<b>2</b>	$50.60 \pm 0.85$	$28.69 \pm 1.18$	$33.65 \pm 1.75$	$38.54 \pm 0.96$
<b>3</b>	$52.49 \pm 1.65$	$26.70 \pm 0.78$	$27.03 \pm 1.10$	$32.11 \pm 1.29$
Cisplatin	$15.18 \pm 1.08$	$12.29 \pm 1.27$	$11.78 \pm 1.52$	$10.29 \pm 1.17$

<sup>a</sup>50%percent inhibitory concentration after exposure for 24 h in MTT assay.

behaviour of **3** is very similar to that of the DNA/BSA binding affinities as discussed previously. Upon ratification of the excellent cytotoxicity properties of complex **3**, further staining assay was conducted with HeLa and HepG2 cancer cell lines to understand the mechanism of action.

#### 3.11.2 | Apoptotic event: AO/EB and DAPI staining

Staining property was investigated to elucidate the basis for the observed induction of cellular death, as it plays a central role in the execution of the apoptotic process. Apoptosis is characterized via DNA fragmentation, chromatin condensation and marginalization, membrane blebbing, cell shrinkage and chromosomal DNA fragmentation of the cells into membrane-enclosed vesicles or apoptotic bodies and global mRNA decay.<sup>[49]</sup> Activity is significantly enhanced in the particular cell lines tested, being clear at 24 h for HeLa and HepG2 cells. To detect cell death at a basic level, microscopic evidence for apoptosis was obtained using AO, EB and DAPI staining, the fluorescence patterns for which depend upon viability and membrane integrity of cells. During morphological analysis using AO/EB and DAPI staining method it can be observed that cell death increases due to cell membrane disruption with an increase in the concentration of each drug, as nuclei appear light orange with a greenish background.

The morphological changes of images of the control cells and treated HeLa and HepG2 cancer cells are depicted in

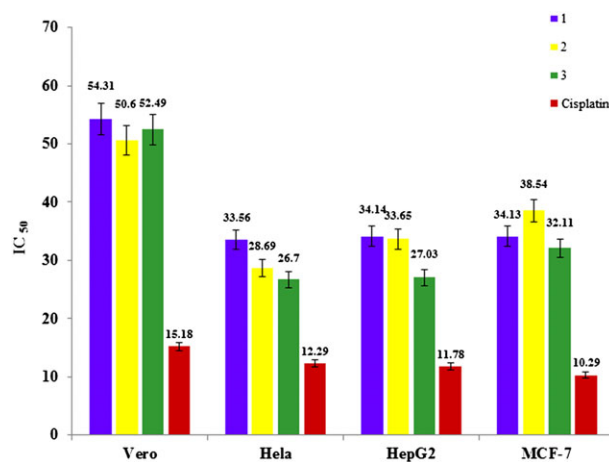
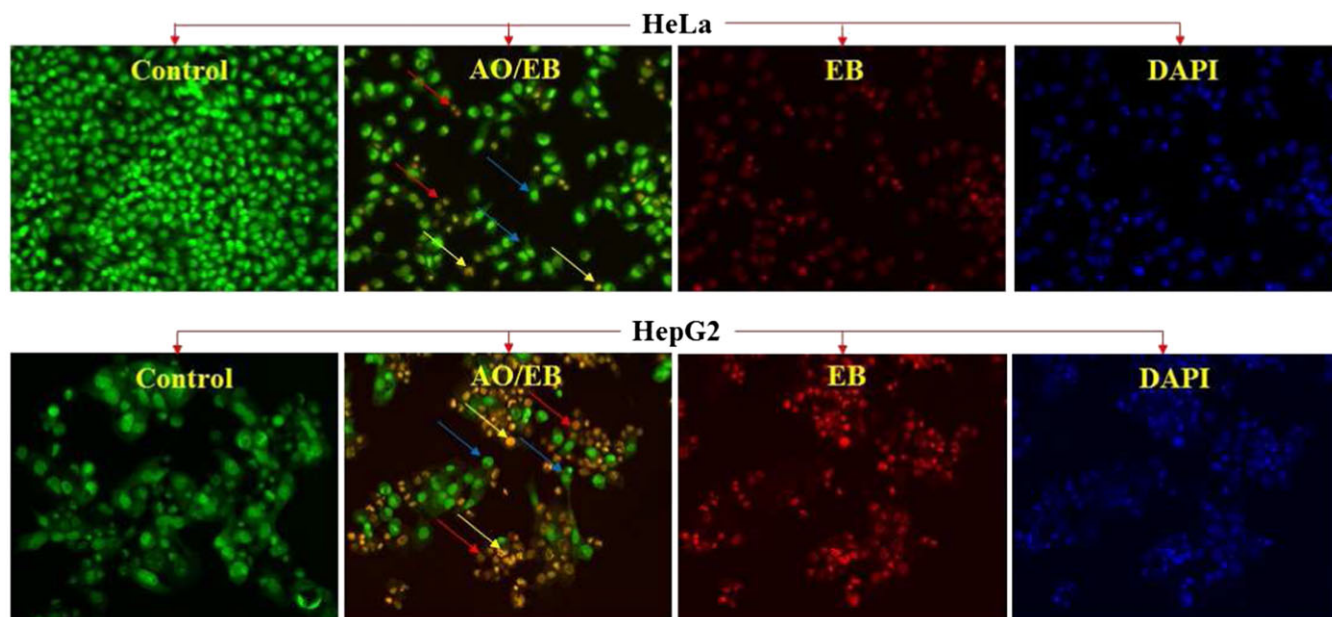


FIGURE 13 Cytotoxicity of complexes **1–3** after 24 h incubation with normal Vero and cancer cell lines MCF-7, HeLa and HepG2



**FIGURE 14** Images of HeLa and HepG2 cancer cells after AO/EB, DAPI and EB staining, incubated for 24 h with treatment by complex **3** with fixed concentration. The yellow arrows show early apoptotic cells with blebbing, blue arrows show late apoptosis and red arrows show necrotic cells

Figure 14. In this figure, yellow arrow(s) show early apoptotic cells with membrane blebbing which is seen at fixed doses ( $10 \mu\text{g ml}^{-1}$ ) of complex **3** and blue arrow(s) indicate late apoptotic cells with chromatin aggregation that is highly condensed chromatin. The red arrow(s) show necrotic cells. These results clearly suggest a mechanism of action of complex **3** which induces necrosis in HeLa and HepG2 liver cancer cells favouring an apoptotic pathway.

#### 4 | CONCLUSIONS

In this work, ligands **H<sub>2</sub>L<sub>1</sub>** and **HL<sub>2</sub>** having different structural features as regards ruthenium(II) and copper(I) precursors and new complexes **1–3** have been synthesized and were characterized using various spectral, analytical and X-ray crystallographic techniques. The new ligands exhibited ONS-tridentate coordination mode for **1** (in a dianionic form) and S-monodentate coordination mode for **2** and **3** (in a neutral form). The coordination mode is governed by hydrolytic cleavage of C=N bond in the benzamidine ligands by metal precursors. The coordination geometry of complexes **1** and **2** was designated as distorted octahedral around ruthenium ion and tetrahedral geometry was assigned for complex **3**. According to the DFT studies, a HOMO–LUMO energy gap evident for the charge transfer interactions occurred within the molecules, as well as a lowering of the band gap. The structural parameters of the compounds that are in good agreement with results of X-ray analysis were obtained by theoretical calculations. The new complexes **1–3** have been used to study their binding properties with CT-DNA/BSA. From the results obtained using fluorescence titrations and EB competitive assay, it was concluded that all complexes

undergo intercalative binding with CT-DNA. Furthermore, the protein binding results revealed that the complexes showed high binding affinity with BSA and quenched the fluorescence of BSA through a static quenching mechanism. For all the complexes, from a strong piece of experimental evidence, the difference of the driving force for the reduction of the metal centres plays an important role in the oxidation of the model substrate 3,5-DTBC and the hydrolysis of 4-NPP in DMF in oxygen atmosphere. Almost all the complexes showed significant cytotoxicity, as evidenced by the submicromolar  $IC_{50}$  values achieved towards various cancer cell lines. The morphological changes of the apoptotic event indicated that complex **3** induces necrosis in HeLa and HepG2 cancer cells favouring an apoptotic pathway.

#### ACKNOWLEDGMENTS

Authors P.V. and P.V. gratefully acknowledge UGC (F. no. 40-66/2011 (SR)) for financial support. R.N. is grateful to DST for financial assistance (project no. SR/FT/CS-95/2010). The Gaussian 09 calculations were carried out in the Wroclaw Centre for Networking and Supercomputing, WCSS, Wroclaw, Poland (<http://www.wcss.wroc.pl>). The authors thank The Director, CAS in Botany, School of Life Sciences, University of Madras, Chennai for providing laboratory facilities to perform the cell line studies.

#### REFERENCES

- [1] H. H. Nguyen, U. Abram, *Eur. J. Inorg. Chem.* **2009**, 21, 3179.
- [2] H. H. Nguyen, J. Grewe, J. Schroer, B. Kuhn, U. Abram, *Inorg. Chem.* **2008**, 47, 5136.
- [3] H. H. Nguyen, U. Abram, *Polyhedron* **2009**, 28, 3945.
- [4] a) L. Beyer, R. Widera, *Tetrahedron Lett.* **1982**, 23, 1881. b) L. Beyer, J. Hartung, R. Widera, *Tetrahedron* **1984**, 40, 405.

- [5] D. Hauenstein, U. Abram, *Inorg. Chem. Commun.* **2011**, *14*, 1262.
- [6] P. I. da S. Maia, H. H. Nguyen, D. Ponader, A. Hagenbach, S. Bergemann, R. Gust, V. M. Deflon, U. Abram, *Inorg. Chem.* **2012**, *51*, 1604.
- [7] a) U. Abram, M. Braun, S. Abram, R. Kirmse, A. Voigt, *J. Chem. Soc. Dalton Trans.* **1998**, 231. b) U. Abram, *Rhenium in Comprehensive Coordination Chemistry II*, Vol. 5, Elsevier, Oxford **2003** 271. c) S. Ritter, U. Abram, *Inorg. Chim. Acta* **1994**, *215*, 159.
- [8] M. M. Sheeba, M. M. Tamizh, L. J. Farrugia, A. Endo, R. Karvembu, *Organon* **2014**, *33*, 540.
- [9] P. I. da S. Maia, H. H. Nguyen, A. Hagenbach, S. Bergemann, R. Gust, V. M. Deflon, U. Abram, *Dalton Trans.* **2013**, *42*, 5111.
- [10] V. Cepeda, M. A. Fuertes, J. Castilla, C. Alonso, C. Quevedo, J. M. Perez, *Anti-Cancer Agents Med. Chem.* **2007**, *7*, 3.
- [11] a) D. S. Raja, N. S. P. Bhuvanesh, K. Natarajan, *Inorg. Chem.* **2011**, *50*, 12852. b) P. Vijayan, P. Viswanathamurthi, V. Silambarasan, D. Velmurugan, K. Velmurugan, R. Nandhakumar, R. J. Butcher, T. Silambarasan, R. Dhandapani, *J. Organomet. Chem.* **2014**, *768*, 163. c) R. Manikandan, N. Chitrapriya, Y. J. Jang, P. Viswanathamurthi, *RSC Adv.* **2013**, *3*, 11647.
- [12] D. S. Raja, N. S. P. Bhuvanesh, K. Natarajan, *Inorg. Chem.* **2011**, *50*, 12852.
- [13] a) W. Hong, H. Lee, T. H. Noh, O.-S. Jung, *Dalton Trans.* **2013**, *42*, 11092. b) P. Vijayan, P. Viswanathamurthi, K. Velmurugan, R. Nandhakumar, M. D. Balakumaran, P. T. Kalaichelvan, J. G. Malecki, *RSC Adv.* **2015**, *5*, 103321.
- [14] *SMART & SAINT Software Reference Manuals*, version 5.0, Bruker AXS Inc., Madison, WI, **1998**.
- [15] M. J. Frisch, G. W. Trucks, H. B. Schlegel, G. E. Scuseria, M. A. Robb, J. R. Cheeseman, G. Scalmani, a. B. Mennucci, G. A. Petersson, H. Nakatsuji, M. Caricato, X. Li, H. P. Hratchian, A. F. Izmaylov, J. Bloino, G. Zheng, J. L. Sonnenberg, M. Hada, M. Ehara, K. Toyota, R. Fukuda, J. Hasegawa, M. Ishida, T. Nakajima, Y. Honda, O. Kitao, H. Nakai, T. Vreven, J. A. Montgomery Jr, J. E. Peralta, J. V. Ortiz, M. Bearpark, J. J. Heyd, E. Brothers, K. N. Kudin, V. N. Staroverov, R. Kobayashi, J. Normand, K. Raghavachari, A. Rendell, J. C. Burant, S. S. Iyengar, J. Tomasi, M. Cossi, N. Rega, J. M. Millam, M. Klene, J. E. Knox, J. B. Cross, V. Bakken, C. Adamo, J. Jaramillo, R. Gomperts, R. E. Stratmann, O. Yazyev, A. J. Austin, R. Cammi, C. Pomelli, J. W. Ochterski, R. L. Martin, K. Morokuma, V. G. Zakrzewski, G. A. Voth, P. Salvador, J. J. Dannenberg, S. Dapprich, A. D. Daniels, O. Farkas, J. B. Foresman, J. V. Ortiz, J. Cioslowski, D. J. Fox, Gaussian 09, Revision A.1, Gaussian Inc., Wallingford, CT, **2009**.
- [16] a) K. Eichkorn, F. Weigend, O. Treutler, R. Ahlrichs, *Theor. Chem. Acc.* **1997**, *97*, 119. b) N. M. O'Boyle, A. L. Tenderholt, K. M. Langner, *J. Comput. Chem.* **2008**, *29*, 839.
- [17] J. S. Casas, M. S. García-Tasende, J. Sordo, *Coord. Chem. Rev.* **2000**, *209*, 197.
- [18] C. Alley, D. A. Scudiero, A. Monks, M. L. Hursey, M. J. Czerwinski, D. L. Fine, B. J. Abbott, J. G. Mayo, R. H. Shoemaker, M. R. Boyd, *Cancer Res.* **1988**, *48*, 589.
- [19] S. Ramakrishnan, V. Rajendran, M. Palaniandavar, V. S. Periasamy, B. S. Srinag, H. Krishnamurthy, M. A. Akbarsha, *Inorg. Chem.* **2009**, *48*, 1309.
- [20] P. Vijayan, P. Viswanathamurthi, K. Velmurugan, R. Nandhakumar, M. D. Balakumaran, P. T. Kalaichelvan, J. G. Malecki, *RSC Adv.* **2015**, *5*, 103321.
- [21] H. H. Nguyen, C. D. Le, C. T. Pham, T. N. Trieu, A. Hagenbach, U. Abram, *Polyhedron* **2012**, *48*, 181.
- [22] N. Ahmed, J. J. Levison, S. D. Robinson, M. F. Uttley, E. R. Wonchoba, G. W. Parshall, *Inorg. Synth.* **1974**, *45*, 15.
- [23] F. H. Jardine, A. G. Vohra, F. J. Young, *J. Inorg. Nucl. Chem.* **1971**, *33*, 2941.
- [24] A. Barandov, U. Abram, *Inorg. Chem.* **2009**, *48*, 8072.
- [25] N. Gunasekaran, R. Karvembu, *Inorg. Chem. Commun.* **2010**, *13*, 952.
- [26] E. Ramachandran, D. Senthil Raja, J. L. Mike, T. R. Wagner, M. Zeller, K. Natarajan, *RSC Adv.* **2012**, *2*, 8515.
- [27] T. Sathiyakamatchi, N. Chitrapriya, H. Lee, C. F. Fronczek, F. R. Fronczek, K. Natarajan, *Dalton Trans.* **2012**, *41*, 2066.
- [28] R. Ramachandran, G. Prakash, S. Selvamurugan, P. Viswanathamurthi, J. G. Malecki, V. Ramkumar, *Dalton Trans.* **2014**, *43*, 7889.
- [29] P. Kalaivani, R. Prabhakaran, P. Poornima, F. Dallemer, K. Vijayalakshmi, V. Vijaya Padma, K. Natarajan, *Organon* **2012**, *31*, 8323.
- [30] J. G. Malecki, I. Łakomska, A. Maroń, M. Szala, M. Fandzloch, J. E. Nycz, *J. Lumin.* **2015**, *161*, 382.
- [31] P. Vijayan, P. Viswanathamurthi, P. Sugumar, M. N. Ponnuswamy, M. D. Balakumaran, P. T. Kalaichelvan, K. Velmurugan, R. Nandhakumar, R. J. Butcher, *Inorg. Chem. Front.* **2015**, *2*, 620.
- [32] R. del Campo, J. J. Criado, E. Garcia, M. R. Hermosa, A. Jimenez-Sanchez, J. L. Manzano, E. Monte, E. Rodriguez-Fernandez, F. Sanz, *J. Inorg. Biochem.* **2002**, *89*, 74.
- [33] H. H. Nguyen, C. T. Pham, U. Abram, *Polyhedron* **2015**, *99*, 216.
- [34] R. Prabhakaran, P. Kalaivani, R. Jayakumar, M. Zeller, A. D. Hunter, S. V. Renukadevi, E. Ramachandran, K. Natarajan, *Metallomics* **2011**, *3*, 42.
- [35] N. Gunasekaran, P. Ramesh, M. N. G. Ponnuswamy, R. Karvembu, *Dalton Trans.* **2011**, *40*, 12519.
- [36] N. Selvakumaran, N. S. P. Bhuvanesh, R. Karvembu, *Dalton Trans.* **2014**, *43*, 16395.
- [37] A. Paul, S. Anbu, G. Sharma, M. L. Kuznetsov, B. Koch, M. Fátima, C. Guedes da Silva, A. J. L. Pombeiro, *Dalton Trans.* **2015**, *44*, 19983.
- [38] R. H. Fish, G. Jaouen, *Organon* **2003**, *22*, 2166.
- [39] Q. Yu, Y. Liu, J. Zhang, F. Yang, D. Sun, D. Liu, Y. Zhou, J. Liu, *Metallomics* **2013**, *5*, 222.
- [40] a) R. Loganathan, S. Ramakrishnan, E. Suresh, A. Riyasdeen, M. A. Akbarsha, M. Palaniandavar, *Inorg. Chem.* **2012**, *51*, 5512. b) G. Prakash, R. Manikandan, P. Viswanathamurthi, K. Velmurugan, R. Nandhakumar, *J. Photochem. Photobiol. B.* **2014**, *138*, 63.
- [41] F. J. M. Almes, D. Porschke, *Biochemistry* **1993**, *32*, 4246.
- [42] Y. J. Liu, Z. H. Liang, Z. Z. Li, J. H. Yao, H. L. Huang, *J. Organomet. Chem.* **2011**, *696*, 2728.
- [43] a) Y. Zhang, Z. D. Qi, D. Zheng, C. H. Li, Y. Liu, *Biol. Trace Elem. Res.* **2009**, *130*, 172. b) J. R. Lackowicz, G. Weber, *Biochem. J.* **1973**, *12*, 4161.
- [44] M. U. Triller, D. Pursche, W. Y. Hsieh, V. L. Pecoraro, A. Rompel, B. Krebs, *Inorg. Chem.* **2003**, *42*, 6274.
- [45] a) J. P. Chyn, F. L. Urbach, *Inorg. Chim. Acta* **1991**, *189*, 157. b) M. Das, R. Nasani, M. Saha, S. M. Mobin, S. Mukhopadhyay, *Dalton Trans.* **2015**, *44*, 2299.
- [46] B. N. Trawick, A. T. Daniher, J. K. Bashkin, *Chem. Rev.* **1998**, *98*, 939.
- [47] K. Du, J. Liang, Y. Wang, J. Kou, C. Qian, L. Ji, H. Chao, *Dalton Trans.* **2014**, *43*, 17303.
- [48] H. L. Huang, Z. Z. Li, Z. H. Liang, J. H. Yao, Y. J. Liu, *Eur. J. Med. Chem.* **2011**, *46*, 3282.
- [49] H. L. Chan, D. L. Ma, M. Yang, C. M. Che, *ChemBioChem* **2003**, *4*, 62.

## SUPPORTING INFORMATION

Additional Supporting Information may be found online in the supporting information tab for this article.

**How to cite this article:** Vijayan, P., Viswanathamurthi, P., Sugumar, P., Ponnuswamy, M. N., Malecki, J. G., Velmurugan, K., Nandhakumar, R., Balakumaran, M. D., and Kalaichelvan, P. T. (2016), Solvent-assisted formation of ruthenium(II)/copper(I) complexes containing thiourea derivatives: Synthesis, crystal structure, density functional theory, enzyme mimetics and *in vitro* biological perspectives, *Appl. Organometal. Chem.*, doi: 10.1002/aoc.3652